TURBULENT BOUNDARY LAYERS AND SEDIMENT RESUSPENSION IN THE ABSENCE OF MEAN SHEAR

A Thesis

Presented to the Faculty of the Graduate School

of Cornell University

in Partial Fulfillment of the Requirements for the Degree of

Master of Science

by

Blair Anne Johnson

January 2012

ABSTRACT

Sediment resuspension is initiated through a variety of mechanisms across the wave breaking, run-up, and run-down stages that occur in the wave breaking, surf, and swash zones. When a wave breaks offshore, the plunging jet rarely reaches the bed directly; however, this injection of momentum generates turbulence that propagates through the water column, creating local stresses as turbulent eddies interact with the seafloor. When these stresses are sufficient to resuspend sediment from the bed, the sediment can become entrained in the flow, and thus both turbulence and sediment are advected shoreward during onshore directed phases of the wave cycle. It is at this time that the fluid is highly turbid, filled with sediment and debris. As the flow enters the swash zone, it runs upshore and slows, and the sediment settles out of entrainment and is deposited onshore. Then, as this relatively clear fluid flow retreats and regains speed in flowing down the beach face, sediment is again resuspended into the flow. But upon careful observation, the turbid region is constrained to the base of the water column due to shear-dominated resuspenions as a boundary layer grows. The resuspension during the latter event can be attributed to an increased bed shear stress, due to the uniform mean flow along the sediment bed. This mechanism for resuspension is well-understood, as thorough experimental research has led to well-characterized parameters such as the Shields Curve that identify requisite shear stresses for sediment resuspension. However, the former mechanism, in which sediment is resuspended due to the interaction of large-scale turbulent motions, has seen far less research, because of the difficulty in isolating this particular flow in the laboratory and identifying

meaningful parameters of the flow necessary for incipient particle motion from the bed.

We have chosen to isolate the phenomenon of sediment resuspension by turbulence absent mean shear in the laboratory to better understand this fundamental process. By adapting a turbulence chamber in the DeFrees Hydraulics Lab developed by Variano & Cowen (2008), in which a Randomly Actuated Synthetic Jet Array (RASJA; Variano and Cowen, 2008) is suspended above a tank of water, with jets directed downward, we have a nearly ideal facility for examining decaying horizontally homogeneous isotropic turbulence above a bed. The jets fire according to a specified random algorithm to generate homogeneous isotropic turbulence without inducing mean flows. With a solid glass bottom boundary in place, data were collected with Acoustic Doppler Velocimetry (ADV) and Particle Image Velocimetry (PIV) measurements to characterize profiles of the mean flow, turbulence intensity, and kinetic energy. Statistics such as spatial and temporal spectra and parameters of mean flow strength were computed to understand the nature of the turbulence in the facility, revealing a well developed inertial subrange and very weak mean flows.. The glass was then replaced with a sediment bed, and the tests were repeated to make a direct comparison between the solid and sediment beds.

During the sediment tests, resuspension was observed intermittently. We were surprised to find that a rippled pattern quickly evolved in the sand bed, even with relatively few visible resuspension events. Preliminary tests have been performed to examine the relationships between the forced turbulence levels and the mechanisms of resuspension, and we have also performed qualitative studies to investigate the influence of the presence of solid boundaries and turbulence on bed morphology. In order to quantitatively analyze the nec-

essary stresses and fluid structures present, a conditional quadrant analysis is performed on the Reynolds stresses.

A small project was included to test the performance of a Nortek Aquadopp High Resolution Profiler in the facility. Though the profiler is designed to capture large-scale environmental flows that are uniform across its beams at a given elevation from its transducer face, this investigation was performed to test the instrument's capability to capture high levels of turbulence in a small facility where this assumption breaks down. Direct comparisons were made to simultaneous PIV measurements, and measurements from the Profiler were included in the overall tank characterization.

BIOGRAPHICAL SKETCH

The author was raised in Kingsville, Maryland, a rural town outside of Baltimore. She began playing the piano at age 3 and later began learning the French horn, both of which she maintained through high school, performing in several school and community orchestras, wind ensembles, and jazz bands. After graduating from Perry Hall High School, the author attended college at Johns Hopkins University to study Civil Engineering. She also studied Piano at the Peabody Conservatory, and received a Minor in Music. During college, the author spent a summer performing Coastal Engineering research in Granada, Spain, and traveling through southwestern Europe. After a college graduation trip to Australia, accomplishing trips to six continents in six years, the author moved to Ithaca, NY, to begin graduate school at Cornell University. The author thoroughly enjoys Ithaca and its gorgeous winters and the opportunities for outdoor adventures year round to complement her studies in Fluid Mechanics. She is looking forward to a few more years of skiing and outrigger canoeing while she works towards her Ph.D. in Civil & Environmental Engineering.

This thesis is dedicated to my family for providing constant support and encouragement.

ACKNOWLEDGEMENTS

In completing this research, I must acknowledge several individuals. Since my arrival in Ithaca, my advisor Todd Cowen has provided answers and insight to frequent questions and confusion in the lab. He is a constant source of inspiration and I am very thankful for his involvement in my studies and work at Cornell. I could not have completed my experimental work without Paul Charles and Tim Brock, who completely redesigned my tank (still without leaks after three years!), and PJ Rusello, who taught me nearly everything I know about the lab. I am grateful to the entire EFMH group for providing daily comic relief, company at lunch, extra hands when lifting large laboratory equipment, and Spanish proofreading and other multi-cultural life lessons. I owe many thanks to Professor Tony Dalrymple for piquing my interest in this field and continuing to provide support beyond my years at Johns Hopkins. Finally, I must acknowledge my family for providing me with so many wonderful opportunities and continuing to support my endeavors.

CONTENTS

LIST OF FIGURES

LIST OF TABLES

CHAPTER 1

INTRODUCTION

1.1 Motivation

Since Osborne Reynolds first conducted dye experiments in the late 19th century, showing the difference between laminar and turbulent pipe flow, scientists have begun to understand the random behavior of turbulence, and its potential effects on mixing and transport. Turbulent flows along flat plates and through channels have seen extensive laboratory experimentation, and they are commonly observed in nature, as unidirectionally flowing rivers or jets, for example. Turbulence is generated from bed shear, and it advects and diffuses through the flow via mean shear and turbulence. In other environmental flows, such as those beneath breaking waves, fluid motion is no longer characterized by flow in a uniform direction, but instead contains velocities with randomly varying directions and magnitudes. In these flows, we can observe stresses that greatly exceed those expected from mean shear flows. Although the interaction of turbulent eddies creates local shear events, as the turbulence becomes more homogeneous and isotropic, the flow does not exhibit mean shear overall. We can thus consider fluid flows to be dominated by either mean shear or turbulence, as environmental flows exhibit a combination of the two flow behaviors.

One particular phenomenon that often accompanies turbulent flows in nature is sediment resuspension, which occurs when a significant fluid stress acting on a sediment-laden bed incites particle motion and lifts sediment grains into the flow. Shear-dominated flows above solid, porous, movable sediment can be recreated in laboratory flumes and analyzed via statistics of the flow and

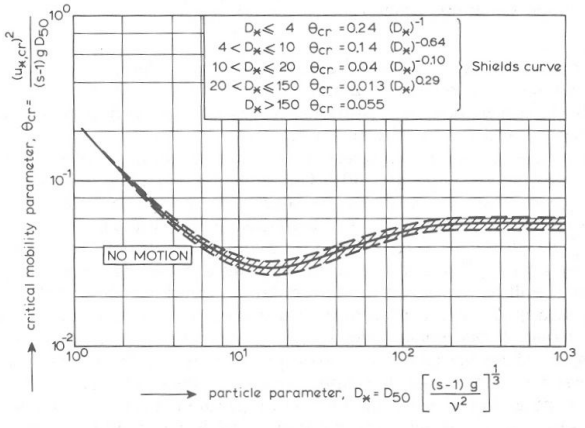

Figure 1.1: Shields Curve, reproduced from van Rijn (1984)

the energy it carries. By observing bed dynamics in these tests, the necessary shear stresses at the bed for sediment motion can be identified as a method of determining which flows will and will not cause saltation or sediment movement at the bed. Such investigations have been compiled into the Shields Curve, a diagram that summarizes the parameterized critical shear stresses required for incipient sediment motion.

The Shields Curve is shown in Figure 1.1, reproduced from van Rijn (1984), nondimensionalized by parameters: critical bed-shear velocity ($u_{*,cr}$), specific density (s), gravitational acceleration (g), particle size (D_{50}), and kinematic viscosity (ν). For scenarios beneath the curves, sediment remains on the bed, whereas points on the curve represent incidents in which sediment grains move very small distances along the bed. Conditions represented by points above the curves are more likely to be resuspended and potentially entrained into the bulk flow, as they illustrate an exceedance of critical stresses for particle motion (van Rijn, 1984).

On the contrary, studies regarding sediment resuspension in highly turbu-

lent flows in absence of mean shear have seen relatively little attention in laboratory research. There is evidence of resuspension in flows in which the energy of the turbulence significantly dominates the mean shear, for instance in the surf and swash zones of beaches. When a wave breaks, momentum is injected into the flow via the plunging jet, which creates a significant amount of turbulence and unpredictable flow patterns. The turbulent energy propagates through the flow and toward the bed through the random motion of eddies, which create temporary and local regions of shear. These intermittent high stress events are sufficient to suspend and entrain sediment, despite the lack of mean shear.

This fundamental process, resuspension of sediment due to turbulence in the absense of mean shear, is challenging to study experimentally, and is thus not as well understood as resuspension in mean shear. By isolating homogeneous isotropic turbulence in controlled laboratory experiments, we can identify the critical parameters of turbulence that cause sediment resuspension, and consequently can develop parameterizations of the turbulent stresses necessary to resuspension, analogous to the critical shear stresses for particle motion summarized by the Shields curve.

1.2 Literature Review

To date, many researchers have considered the challenge of isolating homogeneous isotropic turbulence absent mean shear to induce sediment resuspension. Previous studies have shown a progression in methods of generating laboratory turbulence without mean shear, while simultaneous progress has been made in examining sediment resuspension due to other fluid processes. While these

developments do not thoroughly answer the fundamental research questions proposed, that is, characterizing turbulent boundary layers in absence of mean shear and determining critical structures and stresses responsible for sediment resuspension, the prior investigations provide a worthy history of progress in the field.

1.2.1 Generation of Turbulence Absent Mean Shear

The original laboratory tests developed to study turbulence at the bed in absence of mean shear were performed by Uzkan & Reynolds (1967). Turbulent channel flow was generated by placing a grid at the flume inlet, while mean shear at the bed was, in essence, eliminated by moving the bottom bed at the same speed as the free stream mean water current. Along-stream velocity measurements were recorded using hot wire anemometry. In these experiments, turbulence was found to decay both downstream along the flume, and in proximity to the stationary walls. The bottom boundary layer was characterized by the damping of turbulence intensity that resulted at the moving bed, a quantity found to scale with the viscous lengthscale. It was observed that large eddies were dampened more efficiently than small eddies. With a bed moving at the free stream velocity, there was no additional production of turbulence, and profiles of turbulence intensity were much more constant with a moving wall than with a stationary wall at comparable free stream velocities. Boundary layer thickness scaled with the free stream velocity and distance along the flume from the source of grid turbulence. The resultant profiles of dissipation, turbulence intensity, and other parameters show an important comparison between mean shear and no mean shear at a wall, though they are not precisely the same as

those of homogeneous isotropic turbulence (Perot and Moin, 1995a; Uzkan and Reynolds, 1967).

A similar experiment was performed by Thomas & Hancock (1977), who used moving boundaries in wind tunnels to study turbulent air flows with hot-wire anemometers. The damping at the bottom boundary noted by Uzkan & Reynolds was not observed in the wind tunnel experiment, though a much higher Reynolds number was achieved in the wind tunnel. Reynolds stresses and turbulence intensity profiles showed good agreement with the theory of Taylor's frozen turbulence hypothesis and Hunt & Graham (1978), as did the integral length scales, with the exception of the integral length scale computed from longitudinal velocity records, which was lower than the prediction from theory. The analysis of spectra and effect of the boundary on large and small eddies agreed well with the results from Uzkan & Reynolds (Perot and Moin, 1995a; Thomas and Hancock, 1977).

In 1978, Hunt & Graham considered the prior experiments of Uzkan & Reynolds and Thomas & Hancock, and they verified linear theory with the experimental cases of turbulent flow along a boundary moving at the same speed. They examined relevant scales and important parameters for these different flows, and established a model of turbulent structures near a solid plane boundary. Their analyses also showed varying statistics in each coordinate direction, as the laboratory setups limited the ability to realize isotropic conditions. Qualitative agreement between theoretical and experimental data was found for turbulence intensities in every direction, with the best quantitative agreement normal to the wall (Hunt and Graham, 1978).

Hunt continued this research by further studying the source layer of insta-

bility along the moving bed. Reynolds stresses were considered, as was the balance between the normal components of the Reynolds stress tensor. Hunt discusses the independence of turbulent dissipation with height above the bed for shear-free boundary layers, even though root mean square (r.m.s.) turbulent velocities and turbulent integral scales vary with distance from the bed. Turbulence normal to the boundary faces different scaling restrictions than streamwise turbulence, and it is a function of dissipation and height only within close proximity to the boundary. Horizotal variances were found to increase near the surface, and vertical r.m.s. turbulent velocities decreased to zero toward the surface (Hunt, 1984b).

The preceding analyses explain the role of homogeneous turbulence in a channel without bed shear. Following this experiment-based research, attempts were made to more carefully remove mean flows from turbulence research, and to consider the additional restriction and role of isotropy for comparison to Kolmogorov theory (Kolmogorov, 1941).

Perot & Moin (1995) used DNS to study turbulence at a permeable wall and at a free surface. The work emphasizes the occurrence of splats and antisplats, the coherent fluid eddy structures that interact with boundaries through which they cannot pass. As a parcel of fluid travels towards a wall, it must turn from traveling wall-normal to wall-parallel. This is known as a splat. An antisplat, on the contrary, describes the ejection of a near-boundary parcel back towards the bulk of the flow, an event that typically occurs at the intersection of two adjacent splats. While these events show a transfer of kinetic energy from vertically dominant to horizontally dominant (and vice versa), Perot & Moin argue that it is the imbalance of splats and antisplats, not the individual processes themselves, that

are responsible for this intercomponent energy transfer. They note the difficulty in accurately modeling these flows because of the boundary effects, and discuss the importance and differences of solid, permeable, and free-surface boundary conditions (Perot and Moin, 1995a).

Another investigation related to Hunt & Graham's rapid distortion model of 1978 considered dissipation at solid boundaries, performed through DNS by Teixeira & Belcher (2000). Solid boundaries were instantaneously added into shear-free homogeneous turbulent flows. The DNS model was found effective in showing differences in Reynolds stress profiles at free surfaces and against solid boundaries by incorporating viscous effects and considering the interaction of viscous and other timescales pesent in forced and decaying turbulence. Profiles of dissipation and Reynolds stresses were calculated (Teixeira and Belcher, 2000).

1.2.2 Generation of Turbulence in Grid-Stirred Tanks

Following the laboratory tests that minimized bed shear by placing a moving wall along a turbulent flow, a new laboratory approach of creating turbulence was later developed by building a chamber with an oscillating grid that generated turbulence, without the expected mean flow found in flumes. These chambers are generally called grid-stirred tanks (GSTs) and sometimes "shakers" (Tsai and Lick, 1986). They are often built with square bases, with an oscillating grid located near the bottom to study free surface effects, or near the free surface to examine boundary effects. These tanks are expected to generate turbulence that diffuses away from the grid, with negligible mean flow since there

is no uniform driving current. There are a variety of controls to alter the quality of the turbulence, such as the size and shape of the tank, size and spacing of the grid elements, and driving algorithm of the oscillations.

After GSTs had been used by experimentalists to study turbulence at solid stationary boundaries with the assumption that no mean flows were generated in the facility, Thompson & Turner (1975) saw the opportunity to study the facility to evaluate the qualities of the assumed homogeneous isotropic turbulence and determine whether mean flows actually existed in the tanks. Thompson & Turner used a rotating hot film probe that reversed directions to take measurements of the fluid velocities through a variety of planes parallel to the grid, rather than simply obtaining point measurements. The reversal of the rotation was intended to prevent the probe motion from inducing a mean circulation. There was a pause following completion of each rotation such that measurements would not be greatly affected by the probe wake, as this was an invasive measurement technique interacting with the fluid. Turbulent energy was measured as a function of distance to the grid and of the driving frequency of grid oscillation and stroke distance over which the grid was displaced. Thompson & Turner considered variations in grid dimensions and cross-sectional size of the grid bars. They found a linear relationship between driving frequency and turbulent velocity achieved in the flow (Thompson and Turner, 1975).

Brumley & Jirka (1987) continued in this manner, examining the behavior of GSTs using a similar method to Thompson & Turner (1975) with an internal split hot-film rotating probe. The geometry of the GST was flipped such that the oscillating grid was located above the bottom of a square tank to study free-surface effects. Spatial spectra were computed to determine integral lengthscales, found

to vary with distance from the bed in the "surface-influenced layer," and with the inverse of distance from the grid elsewhere in the flow. Dissipation was computed assuming local isotropy of the turbulence. Despite assumptions of isotropy, there was no experimental verification of isotropic turbulence in the facility or near the surface in particular. Experimental results showed good agreement to Hunt & Graham (1984) when profiles were appropriately non-dimensionalized by the r.m.s. velocities and other statistical parameters of the flow that were approximated from the Hopfinger-Toly relations, which characterize turbulent velocities according to the size and spacing of the grid, and frequency of oscillations (Brumley and Jirka, 1987).

In 2004, McKenna & McGillis examined the generation of mean flows within GSTs, and they also challenged the repeatability of experiments in GSTs. The facility closely resembled the tank used by Brumley & Jirka (1987). They used acoustic Doppler velocimetry (ADV) to collect velocity measurements, from which it was determined that wait time between experiments affected flow behavior, with mean flow velocities varying up to 25% and turbulent fluctuations varying up to 15% for consecutive tests with the same forcing parameters, thus challenging the accuracy of prior GST data that was recorded without sufficient time for the fluid motions to settle prior to the inception of a new experiment. Furthermore, by taking both spatial and temporal Particle Image Velocimetry (PIV) measurements, flow visualizations throughout the tank were analyzed and showed that mean flows existed in large sections of the tank. Since PIV measurements are collected externally, there was no influence of measurement probes in tank flow dynamics, as previous internal probes may have caused. For different forced turbulent flow conditions, there were significant organized mean flows and return flows, challening the notion that GSTs were producing

homogeneous near-isotropic turbulence in absence of mean shear throughout the facility. Other researchers have handled this inhomogeneity by averaging over the entire experimental region, as they saw these mean flows to be insignificant, neglecting to make the measurements that McKenna and McGillis completed to determine how common they actually are. While averaging does negate the effects of mean flows in statistical analyses, there are indeed shear forces created by these mean circulations in the physical flow of the GST. Because of this, GST measurements are possibly skewed, and boundary profiles or other statistical quanities of interest are not necessarily the result of pure turbulence. Though GSTs provide a reasonable generation of homogeneous turbulence, they require alterations of structure or driving algorithms to satisfy the goal of eliminating mean shear in turbulent flows (McKenna and McGillis, 2004). Furthermore, it is not clear whether GSTs have enough degrees of freedom to achieve the generation of homogeneous isotropic turbulence in absence of shear (Variano and Cowen, 2008).

1.2.3 Sediment Resuspension in Grid-Stirred Tanks

Tsai & Lick developed a portable cylindrical GST in order to examine sediment resuspension in turbulence absent mean shear. They did not investigate the turbulence properties of the particular tank, but instead calibrated the tank according to the oscillating frequency required to suspend an equivalent concentration of sediment to a concentration of sediment that could be suspended in a flume with a known applied shear stress. With this calibration of oscillating frequencies to equivalent shear stresses, they could transport the device on ships and extract reasonably undisturbed sediment cores from the bed, and determine the

equivalent stress necessary to resuspend a given concentration of sediment (Tsai and Lick, 1986).

Sanchez & Redondo (1998) recognized strengths of the GST to study sediment resuspension, in particular, the likelihood of sediment to remain entrained in flow following resuspension from the bed. They considered suspended sediment concentrations that they calibrated to images of known sediment concentrations to determine the mass flux possible from a given turbulent r.m.s. velocity. The r.m.s. velocity was calculated from prior formulae developed by Turner (1968) based on the physical geometry of the GST and driving parameters of the oscillating grid (Turner, 1968; Sanchez and Redondo, 1998).

Medina, Sanchez, & Redondo (2001) continued the work with the GST to study initiation of sediment motion due to turbulence to determine whether the turbulent r.m.s. velocity compared with the critical velocities identified by the Shields curve. By placing a thin layer of uniform sand at the bed of the GST and altering the forced flow conditions until sediment was in suspension, they determined the turbulent r.m.s. velocity for sediment resuspension. It seems that the sediment was already in suspension when the r.m.s. velocity was determined, and so incipient motion was not necessarily the standard for selecting the critical GST parameters from which r.m.s. velocities were determined for each sediment grain size. In comparing these critical turbulent r.m.s. velocities of sediment suspension with critical Shields velocities for incipient sediment motion, the Shields velocities are consistently higher than GST r.m.s. velocities by 25-50% (Medina et al., 2001).

Redondo et al. (2001) continued the work further, comparing prior laboratory investigations to experiments with actual sediment cores that they tested in

both the GST and in a channel with turbulent shear flow. Again, turbulent r.m.s. velocities considered for resuspension were notably less than velocities required for incipient particle motion due to shear. It was stated that for the GST, isotropy was an important factor in using such a facility to study this fundamental process; however, a verification of isotropy in the given GST was not presented in the research, again contradicting the arguments of McKenna & McGillis (Redondo et al., 2001).

A characterization of GSTs and verification of GST theory was not explicitly shown in the previous works, despite assumptions of homogeneity and isotropy in many statistical analyses. Furthermore, these studies did not evaluate GST flow structures, despite the strong assumptions that the facilities did not produce mean flows. The experiments of McKenna & McGillis (2004) later showed a lack of isotropy and a presence of mean flows within GSTs in general. Thus earlier data has been slightly misinterpreted, as the shear forces from mean currents within the flow were not considered in subsequent calculations. Additionally, there are not direct measurements of velocities in the tank or near the bed in the experiments of Medina et al. (2001), only empirical calculations of fluctuating velocities that arise from the tank geometry and grid oscillation parameters.

Orlins & Gulliver (2003) also used a GST to study sediment resuspension. They used a laser Doppler velocimeter (LDV) to collect measurements of vertical and horizontal velocity profiles. Non-uniform, partly cohesive sediment from Louisiana was placed in the bed, and water samples were regularly taken from the tank to determine the suspended sediment concentrations as experiments progressed in time. The authors note strong vertical motions in the tank,

as a response to the vertical forcing of the grid. Reynolds stresses ($\overline{u'w'}$) were measured to have an average of zero and absolute value on the order of $10^{-4}\frac{m^2}{s^2}$. The Reynolds stress was constant with vertical height. Turbulent r.m.s. velocities were calculated according to the Hopfinger-Toly relationship and were used to compute turbulent kinetic energy profiles. Suspended sediment concentrations were compared with turbulent kinetic energy levels to determine the energy required to maintain sediment entrainment responsible for mass fluxes that can be related to natural systems (Orlins and Gulliver, 2003).

1.3 Objectives

In the DeFrees Hydraulics Laboratory at Cornell University, we have designed a new laboratory facility to generate horizontally homogeneous near-isotropic turbulence in absence of mean flow. The tank has several adjustible parameters to create turbulence with various energy levels, and length and time scales. By adapting the tank forcing functions, we can examine the interaction of high Reynolds number turbulence against a solid glass boundary with minimal flow, a difficult task to achieve accurately in other facilities. Using PIV, ADV, and other devices and techniques, the flow throughout the tank can be characterized through statistical analysis of the various flow conditions.

By replacing the solid boundary with sand, the tank is an excellent setting to analyze the turbulent boundary layer against a porous sediment boundary. Similar driving conditions can be tested in order to observe the differences between a solid and porous boundary in the presence of forced homogeneous shear-free turbulence. Fluid structures actively interact with the sediment boundary, and

they may pass through porous regions of sand. Turbulent structures in the flow cause the bed to deform in time, and the flow consequently responds to these alterations in bed structure. In a direct comparison between solid and sediment boundaries, there are many contrasting features to explore in both bed and fluid.

Furthermore, by having a non-cohesive sediment boundary, resuspension is an important phenomenon to consider, as it is the primary motivation for this research. Since turbulence can be isolated in the laboratory with this facility, the statistics of the turbulent flow can be evaluated to identify the characteristics of the turbulent flow required to resuspend sediment. By considering Reynolds stresses and turbulence intensities near the bed, and the length scales of the forced flow, we can determine a parameterized turbulent stress responsible for sediment motion, similar to the requisite shear stresses detailed in the Shields Curve.

In addition to the objectives outlined above, an unforeseen goal of this experimental work arose after the work had already begun. Due to the sediment interactions with fluid eddies, the originally flat sand bed evolved into ripples, showing an organized pattern with consistent ripple size and spacing. Ripples and dunes have been shown to be a result of shear events, and so the deformation of the bed into a rippled pattern was very surprising. Similar patterns have been observed in nature, but rarely if ever attributed to turbulence. This is a phenomenon that has been considered in the current research, and it will be further investigated, to evaluate which parameters of the forced turbulent flow and tank geometry or presence of solid boundaries influences bed evolution.

CHAPTER 2

EXPERIMENTAL SETUP AND LABORATORY TECHNIQUES

2.1 Experimental Setup

The laboratory facility has a square base 82cm x 82cm, with a height of 100cm. Three of the walls are glass, and the fourth wall is plexiglass with a side port that provides access to the interior of the tank. The bottom of the tank is an acrylic plate, which shows some minor curvature when the interior of the tank is filled with water. A photograph of the facility is shown in Figure 2.1.

For experiments examining turbulence against a solid boundary, a piece of $\frac{1}{2}$" glass is placed above the acrylic so that the glass surface remains flat and stable, and is elevated approximately 8cm above the tank base, enough to be fully visible in profile during data collection from the exterior of the tank. There is a small gap between the edge of the glass and the side walls of the tank that measures less than $\frac{1}{4}$". For experiments with a sediment boundary, the glass base is removed and replaced with 8cm of sand.

The Randomly Actuated Synthetic Jet Array (RASJA), the structure that generates the turbulent forcing, is suspended above the top of the tank. The array contains an 8x8 grid of jets spaced at 10cm on an acrylic sheet that can be raised or lowered as one possible means of altering the state of turbulence in the tank interior, both by affecting the tank volume and the distance over which the individual jet flows can interact. Figure 2.2 shows the mechanism for raising and lowering the jets. This consists of four threaded rods that cross the top of the tank. The jets remain submerged underwater on the acrylic panel, which has

Figure 2.1: Photo of RASJA and ADV in turbulence tank

holes and outlets to the free surface above, through which instruments can be placed, though this surface generally acts as a rigid lid. The array can also be tilted to allow access to the bed without removing the array or draining the tank. During experiments, the edges of the array are shimmed to limit vibrations of the array, as there is a 1cm gap between the array and the walls of the tank.

Very near to the jet orifice plane at the top of the tank, it is expected that local flows are dominated by the on/off state of the nearest jet. Below this region, the flow mixes into a layer of homogeneous, nearly isotropic turbulence. Fluid motions are no longer influenced by the state of adjacent jets, in essence unaware of the overlying jet firing pattern above. Beneath this merging region, flow is affected only by the presence of the bottom boundary, and results in decaying horizontally homogeneous turbulence. These regions are summarized in Figure 2.3.

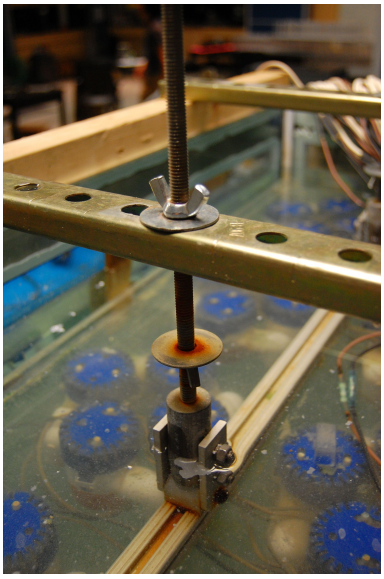

Figure 2.2: Photo of RASJA adjustible suspension mechanism

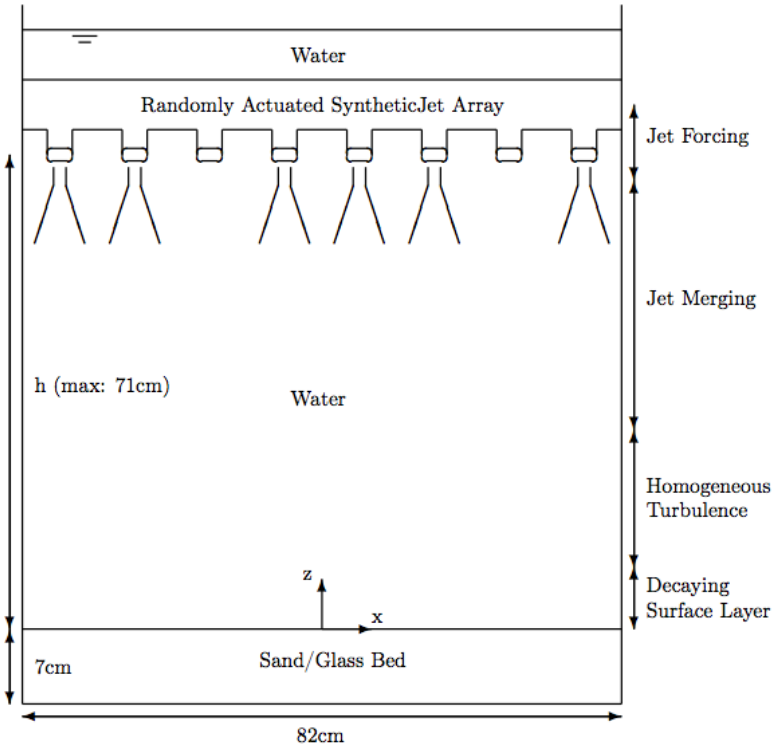

Figure 2.3: Sketch of Experimental Facility with Flow Structure

2.2 Generation of Turbulence

The RASJA was developed by Variano, Bodenschatz, and Cowen (2004) to study free surface effects in decaying homogeneous isotropic turbulence. The 64 jet array was constructed by mounting 12V bilge pumps to the 80cm by 80cm acrylic support and connecting 2.19cm elbow PVC joints to the pumps, so that each jet of water is directed perpendicular to the acrylic support panel. The RASJA was originally mounted from the bottom of the tank, so that the jets would direct water upward, creating a layer of homogeneous isotropic turbulence within approximately 20cm the free surface. At that time, the tank had a square base 80cm on a side, with a height near 1m (Variano et al., 2004).

Variano developed an algorithm so that the 64 jets fired quasi-randomly to generate maximal homogeneous isotropic turbulence without inducing a mean flow or inefficiently firing more jets than necessary. It was found that when running 12% of the jets, each jet with a mean on-time of 3 seconds with a standard deviation of 1 second, the maximum level of homogeneous isotropic turbulence was produced (Variano and Cowen, 2008). The distribution of jet on-times is Gaussian with truncated tails, so as not to result in negative on-times. The instantaneous state of the entire RASJA changes as often as every 0.375 seconds. Following Variano's work to study free-surface gas effects, the tank was reconstructed with a slightly larger side length of 82cm. The same array of jets is used to generate turbulence from the top of the tank, so that the region of homogeneous isotropic turbulence is presently near the bottom 30% of the tank to study boundary layer effects. The 12% firing algorithm is generally maintained, with occasional adaptations to alter the interaction of the turbulence with the side walls and to study the fluid behavior under various forcings. A thorough

characterization of the tank is included in Chapter 3 to verify that the new configuration performs similarly to an upside-down version of Variano's original tank.

2.3 Experimental Considerations

Working with fluid processes that generate resuspension of sediment, decisions were made on how to best select a representative sediment and design experiments that allow for straightforward observations and a multitude of methods to collect data. For the current project, we elected to study sand as is it relatively uniform in shape and is not cohesive. We also needed to seed the flow with neutrally buoyant particles so that acoustic and optical measurements could be made.

2.3.1 Sand

Everlast commercial playsand was selected as the representative sediment. The sand was shaken through a #30 sieve with 600μm openings to eliminate stones and debris, then it was thoroughly and frequently washed to remove fines. Periodically, the sand was rinsed and sieved again to remove additional particles that accumulated in the tank, from flocculated seeding particles, algae, or degraded rubber pieces from laboratory hoses and instruments. After being rinsed and sieved, the sand is very uniform in size, with 50% exceeding a diameter of approximately 260μm according to a linear interpolation of the distribution shown in Table 2.1. When it is in the tank, it is filled to a depth of approximately

Diameter (μm)	Percent passing
75	0.1
106	1.6
212	45.6
425	93.1
600	100

Table 2.1: Sand Grain Distribution Analysis

8cm, and so the underlying solid acrylic bottom of the tank can be neglected as having a solid boundary influence.

Prior to experiments, the sand bed is raked and flattened at the sediment-water interface to diminish prominent peaks, ripples, and scour holes that develop during previous tests or experimental set-up procedures. Although the surface of the sediment is often not perfectly flat, slight imperfections in the initial state typically tend to disappear quickly after the jets are turned on. However, larger deformations up to 3-4cm in height tend to develop if the bed is not smoothed, thus leading to inconsistent boundary conditions among tests.

2.3.2 Seeding Particles

To appropriately seed the tank with neutrally buoyant particles, we selected Arkema Group ORGASOL (R) 2002 ES 3 Nat 3 Polyamide 12, a nylon particle with an average batch diameter of 29.4 μm, with 5% less than 20 μm and 8% greater than 40 μm, and with a specific gravity of 1.03. This particle is appropriate for ADV measurements using 20°C water, sampling at an acoustic frequency of 10MHz. The same particles are used as acoustic scatterers for measurements

made with a high-resolution acoustic current profiler, and to scatter light and act as visible flow tracers when recording PIV data. Calculating the settling velocity V_s, relaxation time τ, and Stokes number S_k according to:

$$V_s = \frac{2}{9}(\frac{\rho_p - \rho_f}{\mu})gR^2$$

$$\tau = \frac{\rho_p D^2}{18\mu}$$

$$S_k = \frac{\tau V_s}{D}$$

where ρ_p and ρ_f represent particle and fluid densities, respectively, g is gravitational acceleration, R and D are particle radius and diameter, respectively, and μ is the fluid viscosity, we can determine whether these particles passively follow the flow (Wereley and Nguyen, 2002). We find a fluid settling velocity of $0.14\mu m/s$ and Stokes number of $2.4x10^{-5}$. With a Stokes number much less than unity, the particles should accurately adhere to steamlines of the flow with less than 1% error (Tropea et al., 2007).

2.4 Measurement Techniques

A variety of tools have been used to characterize the turbulence tank and to observe fluid and particle motions throughout the flow and along boundaries. It is not an easy task to monitor the entire 3-dimensional flow as it develops in time, so a combination of several instruments and techniques has provided ample information regarding the intricate properties of turbulent flow, its interaction with solid and sediment boundaries, and its ability to resuspend sediment.

2.4.1 Particle Image Velocimetry

With the primary focus of this project involving direct interaction of turbulence with various boundaries, PIV allowed temporally evolving two-dimensional spatial measurements to be recorded at the bottom boundary. For the tank characterization and boundary-comparison experiments, an argon-ion laser was used with a scanning mirror to produce a nearly 10cm by 10cm illuminated field-of-view (FOV) centered in the tank, just above and including the bottom surface.

Images were captured using a Dalsa-Coreco SMD 1M-60 camera with a 60mm Nikon lens. Image pairs were recorded at a 1Hz sampling rate over 30 minute periods. Photos were captured as greyscale 12-bit tiff images. The time Δt between images within a pair ranged from 7ms to 10ms, for glass and sand bottom boundaries, respectively. The time between image pairs was 1s. For the tests with a glass boundary, the tank was seeded with the same Orgasol particles that were used during the ADV measurements. For tests with a sand boundary, both fines from the sand and actual sand grains could be observed as tracer particles in the images, potentially allowing analysis of the fluid and sediment motions separately in the future. After computing particle displacements and velocity fields, turbulent characteristics such as spectra, turbulent intensities, and other statistics were computed across the FOV.

PIV images also provided insight into isolated flow events, such as vertical resuspension episodes and sediment entrainment into the flow, as there is a marked distinction between sediment and fluid seeding particles in the images, as seen in Figure 5.14, in which very bright particles are sand grains, and faint particles are the tracers. Though the measurements were made across a

Boundary:	Glass	Sediment
FOV: height x width (cm)	8.84 x 9.45	9.09 x 10.02
FOV (pixels)	928 x 992	900 x 992
Pixel Calibration (cm/pix)	1/105	1/99
Δt (ms)	7	10

Table 2.2: PIV Image Collection Parameters

2-D cross-section, due to symmetry of the tank and verification from ADV measurements, we have assumed that statistics in the x- and y- directions are equal, if x and y are taken as the bed-parallel, wall-orthogonal coordinate directions, resulting in a quasi 3-D measurement region.

Image Analysis

The analyses of the images were performed in Qian Liao's Matlab implementationf of Cowen & Monismith (1997) and Liao & Cowen (2005). Table 2.2 shows the parameters used in analyzing the image pairs for the standard boundary characterization tests. Liao's code was at times susceptible to crashes or termination of Matlab, so particular parameters were set to run the code correctly. A summary of these analysis parameters is presented in Table 2.3. With these parameters in place, the 1024x1024 pixel images were cropped slightly, to capture the bed and approximately 9cm of flow above the bed. As with any PIV algorithm, peak-locking is present, but fortunately Liao's code has a function in place to diminish the effects of peak-locking on integer pixel displacements (Liao and Cowen, 2005). This is evident in the sample histograms shown in Figure 2.4, computed above a glass bed with a jet height H=71cm.

Iteration:	1st pass	2nd pass
subwindow size (pixels)	64x64	32x32
subwindow overlap	50%	50%
minimum correlation coefficient	0.15	0.10
sub-pixel method	0	0
max pass	6	6

Table 2.3: PIV Analysis Code Parameters

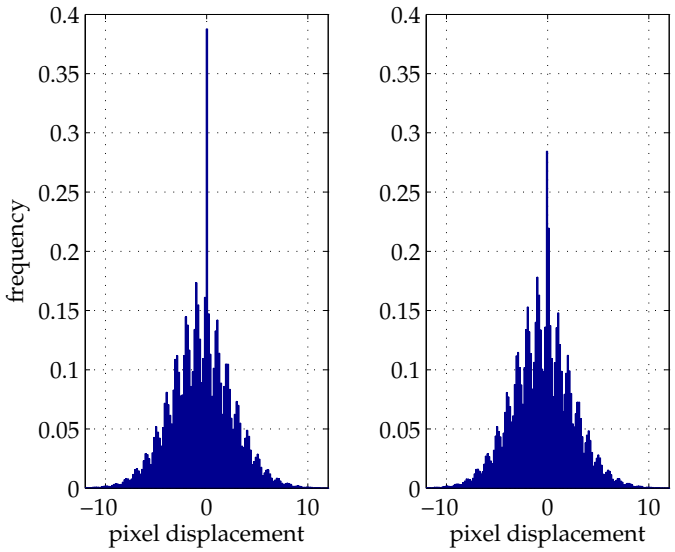

Figure 2.4: Histogram of pixel displacements and minor peak-locking before (left) and after (right) removing unconverged and filtered data

Data Quality Control and Interpolation

In the image analysis, there are two filters in place. Converged velocity vectors are compared to surrounding velocity vectors, and those velocity vectors that deviate significantly from their neighbors, defined as being more than 1.5 standard deviations from the mean value of surrounding vectors, are replaced with the median of the 4x4 or 3x3 array of surrounding vectors, according to the

Medfilt2 function in Matlab. This is known as local median filtering. Unconverged vectors are replaced with a value of zero. Only the directly computed converged valid vectors are used; the replacement median values and zero values are ignored. Figure 2.5 shows the percentage of valid vectors in the data taken above a glass bed at a jet height of H=71cm, that is, the percentage of data that came directly from Liao's PIV code that produced a converged vector that had not been affected by the local median filter. Evidently, approximately 90% of the data is good, and sufficient for calculating energy and other quantities to characterize the flow. The histograms in Figure 2.4 show the difference before and after removing these unconverged (zero) and median-filtered points from the data. Both of the histograms are with the anti-peak-locking filter applied. In the histogram on the right, there remains a fairly significant peak at zero, but this is only for the values of zero directly at and above the bed. The frequency of zero-pixel displacements drops by approximately 10% in the histogram after removing all of the unconverged vectors that were replaced with a value of zero; this complements the valid vector fraction figure, in which 90% of the data was shown to be valid.

Only when computing statistical metrics, such as velocity spectra, that require complete temporal and spatial records do we use spatial interpolation schemes to replace spurious vectors in the velocity fields. The Matlab function TriScatteredInterp was used to interpolate the missing data by using Delaunay triangulation with linear interpolation. As this method only interpolates interior data, and does not extrapolate missing boundary values, missing corner values were assigned values equivalent to the mean of the existing corner data, and thus TriScatteredInterp was sufficient to fill in the missing values.

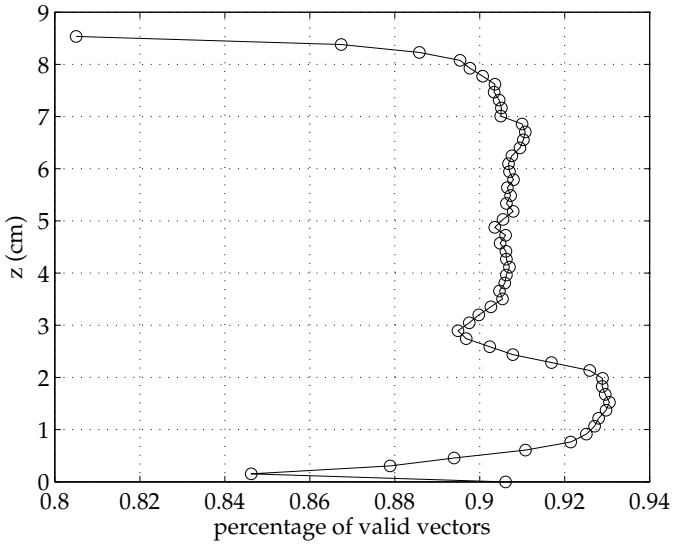

Figure 2.5: Valid vector fraction

2.4.2 Acoustic Doppler Velocimetry

To quantify turbulence statistics throughout the depth of the tank, ADV measurements were made using a Nortek Vectrino along a profile centered horizontally within the tank, as shown in Figure 2.1. Samples were recorded at 50Hz for 40 minutes at each height considered, from near-bed measurements to 50cm above the bed. An additional ADV dataset was collected near a side wall in order to examine side-wall boundary affects and determine whether significantly different flows existed near the walls as compared to the boundary-free tank center. The measurement was 8.6cm away from the wall, and approximately 10cm above the bed. In collecting ADV data, Table 2.4 summarizes the measurement parameters set for each of the experiments, the results of which are shown in Section 3.1.1.

Measurement	Heights (cm)	Sample Volume (mm) / Transmit Length (mm)	Velocity Range (cm/s)
Through-Tank	0.4 -5.0	6.4 / 1.2	30
Through-Tank	10.0 - 55.0	7.0 / 1.8	30
Near-Bed	0.5 - 1.8	7.0 / 1.8	30
Near-Bed	2.2 - 2.6	7.0 / 1.8	100
Near-Bed	3.0 - 3.5	7.0 / 1.8	30
Near-Bed	4.0	6.4 / 1.2	100
Near-Wall	10	7.0 / 1.8	30

Table 2.4: ADV Measurement Settings

2.4.3 High-Resolution Current Profiler

During a three month loan from NortekUSA, an Aquadopp High Resolution (HR) Profiler was used to record velocity measurements along linear profiles through the tank. The HR Profiler is an acoustic device like the ADV. It has the advantage of recording in both space and time, though velocity measurements can sometimes only be made in one coordinate direction instead of the three directions captured simultaneously by the ADV, depending on the user-input settings on the instrument. It can also be mounted to record data non-invasively, as measurements can be made significant distances away from the head as long as there are no interfering acoustic barriers between the instrument and regions of interest in the flow. In the laboratory tests, measurements with the HR Profiler were recorded with a sediment boundary in place. Data was sampled at 1Hz for 20 to 30 minute records for all tests. The user-input settings on the instrument software are summarized in Table 2.5.

Parameter	Value
Blanking Distance	10cm
Measurement Volume	7mm
Velocity Range	±13 cm/s
Pulse Distance	90cm
Profile Range	79cm

Table 2.5: Aquadopp Measurement Settings

The instrument has a 90-degree head, such that velocities are measured perpendicular to the instrument body. The three beams that collect data are offset 25 degrees from this perpendicular axis. These geometric considerations had to be noted when mounting the instrument for experiments. When recording velocities along all three beams, a composite three-component velocity profile can be compiled along the perpendicular axis, as the individual beam velocities can be combined using their geometry to approximate the three-component velocity profile on this perpendicular axis. However, the instrument is designed to collect field data in regions significantly larger than an 82cm square test facility; thus in a small environment, this compiled three-component profile is not necessarily representative of the flow since the beams may spread too far to capture relevant flow structures. The HR Profiler was configured to record individual beam velocities, considering only the velocity in the direction of each beam along its path. For most of the test regions considered, this single-beam approach was the most meaningful method for the facility, yet three-component velocity profiles were also compiled to determine whether this instrument can record significant data in turbulent flows and in boundary layers.

During initial tests with the device, vertical profiles centered laterally were

recorded throughout the water column from the jets to the bed, with jet heights ranging from 71cm above the bed down to 41cm, varied in 5cm increments. The measurements were single beam vertical velocities. Figure 2.6 shows the top-mount suspension of the HR Profiler, which is mounted above the tank such that the jet height can be changed independently of the HR Profiler, since there is a hole in the acrylic jet base through which the HR Profiler can collect data, as long as the profiler head remains submerged. The measurements were made within the first 75 minutes of turning the jets on, during which the sand was relatively flat in the center of the tank. These tests were performed in the default jet-firing congifuration in which all of the jets were programmed to run at 12% firing. Two additional vertical profiles were recorded at maximum jet height, in which one or two outer-perimeters of jets in the RASJA were turned off completely, in order to observe fluid motion with diminished side wall interactions.

To evaluate the performance of the HR Profiler in this confined laboratory space, simultaneous PIV images were collected in the same region through which the beam of the HR Profiler passed, so that data could be directly compared to the relatively robust PIV data and be examined for accuracy. Several configurations were tested for these experiments. The HR Profiler was buried in the sand bed for these cases, such that the body of the instrument was level with the sand and the head was exposed for data collection. In one test, the HR Profiler was mounted diagonally in the bed so that a single beam would be in line with a PIV field of view (FOV) close to the center of the tank and the three-component axis was directed vertically upward. This configuration is pictured in Figure 2.7.

In another test, shown in Figure 2.8, the HR Profiler was mounted parallel to

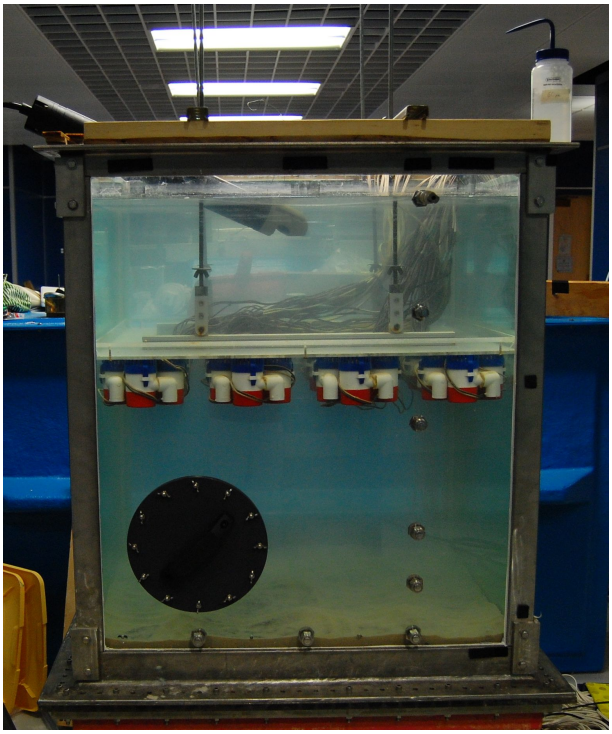

Figure 2.6: Aquadopp HR Profiler suspension for vertical velocity measurements

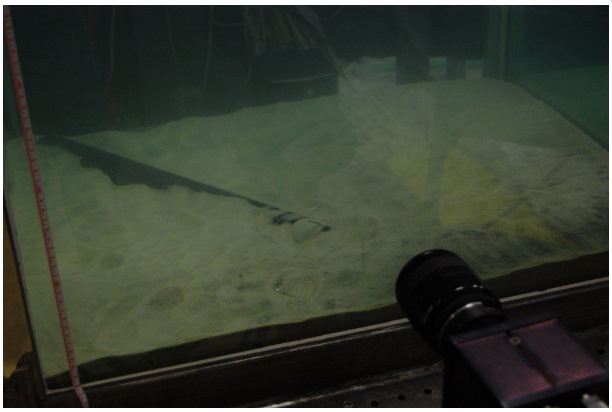

Figure 2.7: Photo of simultaneous PIV with Aquadopp HR Profiler setup for near-boundary beam velocity comparison

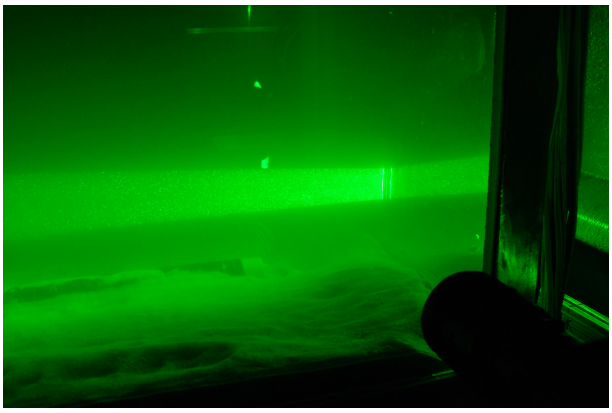

Figure 2.8: Aquadopp HR Profiler setup for simultaneous 2-D PIV velocity comparison velocity PIV comparison

the tank walls such that the instrument body was directly in line with the PIV FOV. In this case, one beam of the HR Profiler passed through the FOV, and the other two beams measured in front of and behind the FOV, so that compiling the three beam velocities would produce a three-component velocity profile parallel to the HR Profiler that passed through the FOV as well. This is the only instance in which the three-component velocity compilation was considered, as it was convenient in this physical configuration to make a direct accuracy comparison to PIV. The region considered in this test was located very close to a side wall of the tank.

2.4.4 Wage Gauges

After initial tests with the RASJA suspended above the bed, spectral analyses of the prominent frequencies shows an unexpected minor peak at approximately 0.03Hz throughout the tank. Thinking this might be due to a tank seiche that could be observed on the free surface above the jet array, Banner Engineering Ultrasonic Wave Gauges, S18U series wave gauges were installed above the

tank to monitor the free surface above the RASJA, as there was slight visible motion in the water despite the nearly-solid acrylic panel that separated the free surface from the turbulent interior of the tank. The frequencies observed with the wave gauges were inconclusive, and they did not agree with those from the spectral analysis of ADV data within the body of the tank. Thus, it seems there is no resonant tank seiche, and that the free surface is indeed sufficiently isolated from the turbulent interior body of the tank by the acrylic base of the RASJA.

2.4.5 Time-lapsed Photography

In order to capture the evolution of the sand bed, which evolved into a rippled pattern after the jets were activated, a Nikon D40 camera was mounted externally to record still photographs of the bed of the tank. Using the application Sofortbild, a recording over a 12-hour period was compiled into a movie of the sand bed evolution. For the first four hours, photographs were recorded every minute, and for the following eight hours, photographs were recorded every ten minutes. Results are presented in Figure 6.1.

CHAPTER 3

DATA ANALYSIS AND TANK CHARACTERIZATION

Since turbulence is a highly random process, it is characterized predominantly through statistical analysis of velocity measurements of the flow. Of particular interest are measurements throughout the bulk of the tank to show the development of turbulence away from the jets, and detailed measurements near the bed to show the decay of turbulence at a boundary. For measurements away from the boundary, ADV measurements are used on a fairly coarse resolution, whereas a combination of ADV and PIV measurements allow for much finer measurements near the bed. In the PIV datasets, resulting profiles are often presented as a function of RASJA height, as experiments were performed with varying RASJA height as a simple way of altering the turbulence levels in the facility. For figures in which the legends have been omitted, the standard legend presented in Figure 3.3 is consistent throughout the remainder of the data analysis, where heights H = 71, 66, 61, 56, 51, 46, 41cm represent jet heights above a solid boundary, and *sand* denotes a jet height of 71 cm above the sediment bed.

3.1 Vertical and Horizontal Velocities

In the turbulence tank, we aim to produce no mean flow. Using ADV and PIV measurements, we can evaluate the performance of the facility by comparing profiles recorded throughout the tank and near the bed.

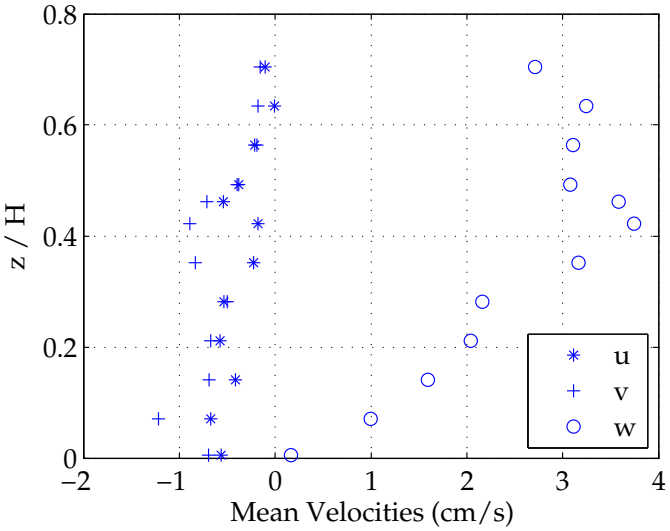

Figure 3.1: ADV measurements of mean velocity profiles throughout depth of tank

3.1.1 ADV Profiles

The profile shown in Figure 3.1 shows the mean velocities recorded at heights throughout the entire tank at 5cm increments, normalized by jet orifice height $H = 71cm$ with both horizontal (u, v) and vertical (w) components measured. We see consisent agreement in the horizontally homogeneous velocity fields, with greater variation in the vertical velocity as the flow is heavily influenced by the local jet-forcing patterns in the upper regions of the tank. The vertical velocity approaches zero near the bed, as expected, due to the kinematic boundary condition, and the horizontal velocity is approximately zero at the bed from the no slip boundary condition.

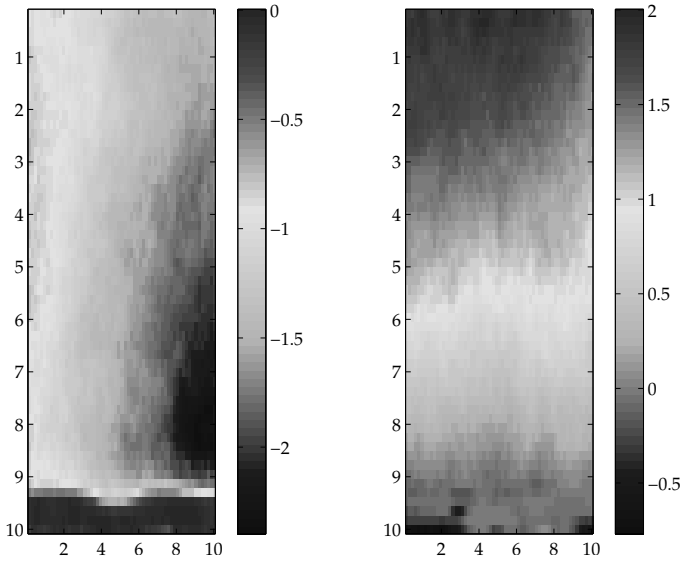

Figure 3.2: Time-averaged velocity fields: $\overline{u}$ (left) and $\overline{w}$ (right); axis labels show FOV location (cm), colorbar gradation shows velocity magnitude (cm/s) for H=71cm above a sediment bed

3.1.2 PIV Profiles

The analysis of the PIV data assumes homogeneity in the horizontal and that the FOV is centered in the tank. Figure 3.2 shows the 30-minute averages of the horizontal and vertical velocity fields recorded over the sediment bed, in which we see a relatively uniform vertical velocity at a given height, though the horizontal velocity field shows weak gradients in both the horizontal and vertical. However, noting that these are small gradients, we will assume horizontal homogeniety for the remainder of the statistical analysis, and comments on inhomogeneities will be discussed in Chapters 5 and 6 regarding local bed structures and sediment resuspension.

The horizontally and time averaged velocity profiles are shown in Figure 3.3, which compares the horizontal (u) and vertical (w) mean velocity profiles. We see results near zero, but with leftward tendencies in the horizontal and upward

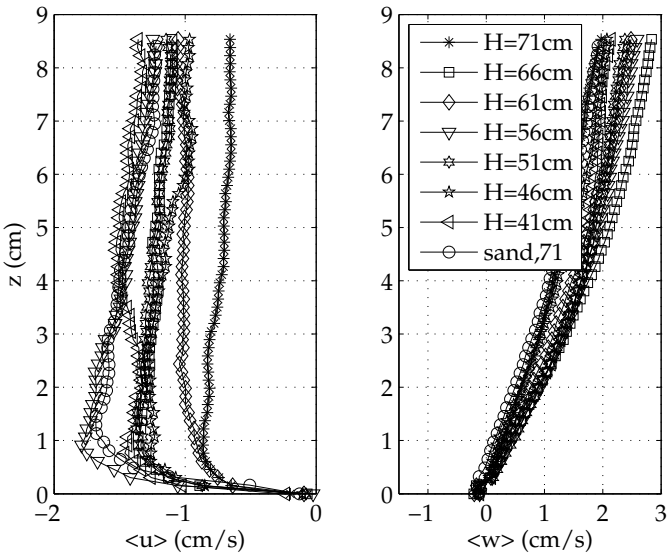

Figure 3.3: Mean Velocity Profiles

tendencies in the vertical fluid motion. There is little correlation between RASJA height and magnitude of velocity; all jet heights result in similarly-shaped profiles, but the magnitudes vary independently. It can be noted that above a sediment bed, the magnitude of the horizontal velocity is much closer to zero than above a solid boundary. The vertical velocity profile also has a near-zero velocity very similar to several of the other velocity profiles above a solid bed.

3.2 Strength of Mean Flow

3.2.1 ADV Profiles

The turbulence tank has been designed to minimize formation of mean flows that exist due to the jet forcing conditions. When averaged across all space, of course the facility would show zero mean flow, as any driven shear flows will

have return flow counterparts elsewhere in the tank. However, it is also a concern that there are no local mean flows or steady circulation patterns existing in the facility that could affect measurements recorded in small spatial locations of interest; thus global averaging will not be performed as a measure of verifying the absence of shear.

In order to determine whether mean flows exist in the tank, we consider the variable M^* (Variano and Cowen, 2008), the ratio of the mean kinetic energy (E) to the turbulent kinetic energy (k), according to the Reynolds decomposition of mean and fluctuating velocity, denoted with an overbar and prime, respectively, such that

$$u(t) = \overline{u} + u'(t)$$

$$E = \frac{(\overline{u}^2 + \overline{v}^2 + \overline{w}^2)}{2}$$

$$k = \frac{(\overline{u'^2} + \overline{v'^2} + \overline{w'^2})}{2}$$

$$M^* = \frac{E}{k}$$

M^* is computed from ADV measurements through the center of the tank. Figure 3.4 plots M^* as a function of measurements heights, z, normalized by jet height, H=71cm. We expect mean flows of zero and also minimal values of M^* in regions of homogeneous isotropic turbulence. In it can be noted that for the bottom 30% of the tank, M^* is less than 10%, a significantly low ratio (Variano et al., 2004).

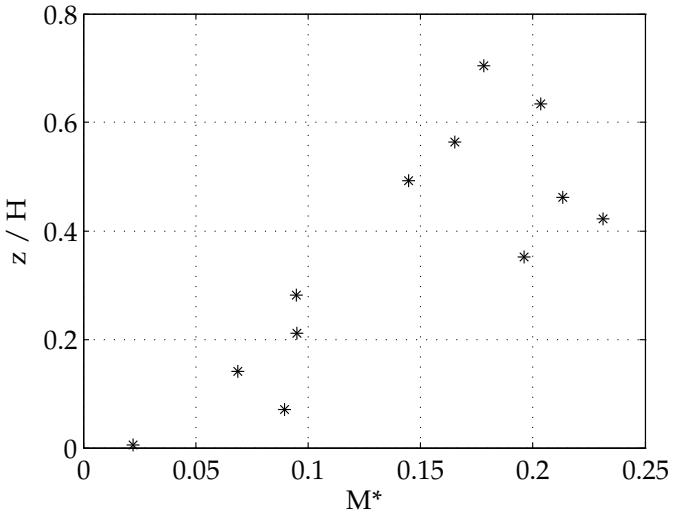

Figure 3.4: Mean flow strength profile through tank

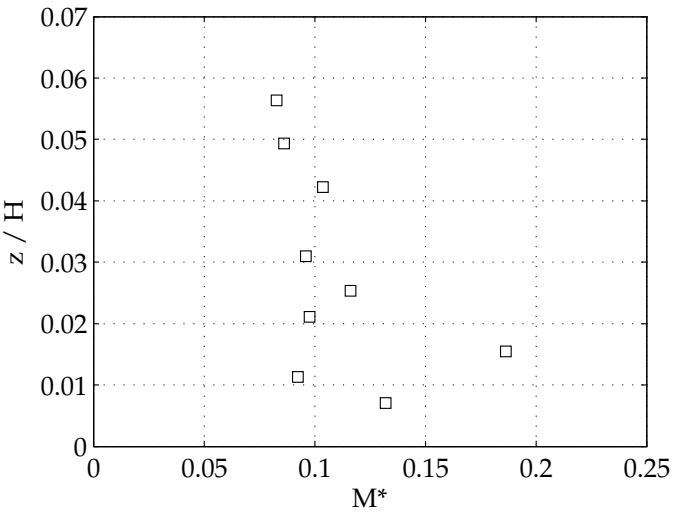

Figure 3.5: Near-bed mean flow strength at a solid impermeable boundary

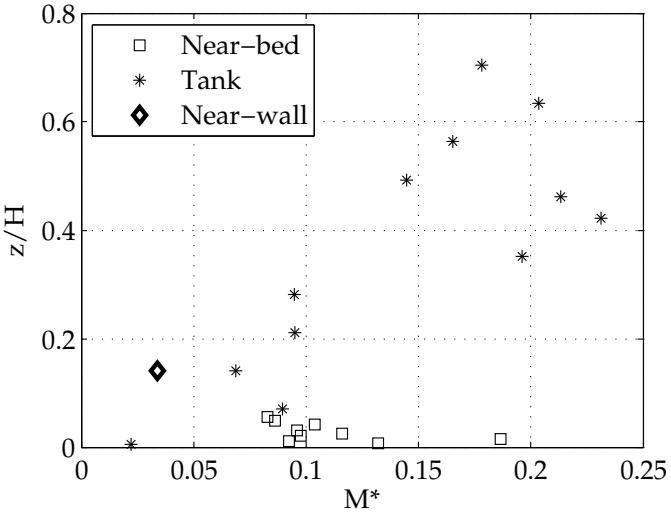

Figure 3.6: Mean flow strength measurements at 3 regions

A more refined profile is shown in Figure 3.5, in which ADV measurements were collected only 3-5mm apart, very close to the bed. This data was collected two months after the initial coarse profile dataset with the solid boundary still in place. Except for two points extremely close to the bed, the values still remain below 10%. An additional single point ADV measurement was recorded above the sediment boundary, in order to do a quick measurement of near-wall boundary effects, which will be discussed in greater detail in Section 6.3. This diamond-shaped data point shown in Figure 3.6 was measured off-center, approximately 10cm above the bed and $10\,cm$ from the wall as a rough determination of significant flows or circulations occur along the side walls. Seeing a value of M^* below 5%, we assume negligible wall effects for the following sections of statistical data analysis, which have emphasis on the bottom boundary near the center of the tank for both solid and sediment boundaries; however, as this is only one measurement near the wall, further investigations are required to ensure minimal near-wall flows.

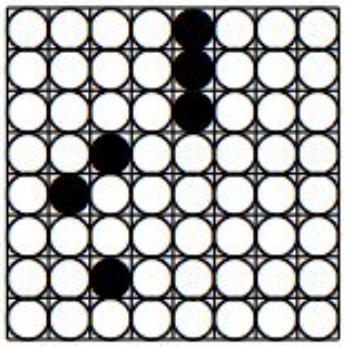

Figure 3.7: Sketch of jet grid array, highlighting location of dead pumps (shown as filled-in circles) among working jets (open circles)

One concern regards the initial state of the tank prior to each set of experiments. We know that following the initial setup in April 2009, when the first ADV tests were completed, and before January of 2010, a total of 6 of the 64 jets ceased to work, due to either dead pumps, blown fuses, or corroded control wires. A diagram of the pumps is shown in Figure 3.7. This shows that two of the dead pumps were quite near to the center, so it is possible that this altered state of firing impacted the homogeneity of the turbulence throughout the tank and affected the strength of the mean flow in an unexpected fashion as shown in Figure 3.3. It is possible that some of these six pumps stopped running prior to the refined measurements, but we cannot determine the former pump configuration retroactively. For future publications and further research, these tests will be repeated in detail, with the pumps repaired. This discrepancy in the data demonstrates the importance of frequently testing the power of the jets, so that all data is representative of optimal tank performance.

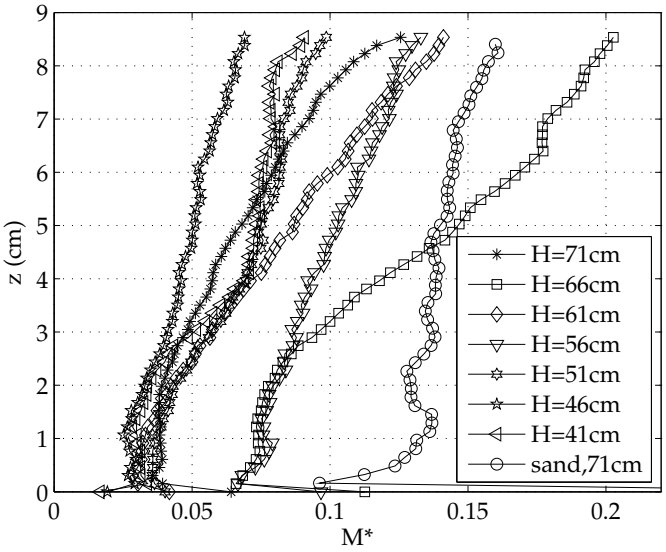

Figure 3.8: Near-bed Mean Flow Strength profiles from PIV data

3.2.2 PIV Profiles

Additional near-bed measurements on a finer resolution have been computed from the PIV data, up to 9cm above the bed, as shown in Figure 3.8. Indeed we see values of M^* less than 10% for most of the profiles, however we see values above 10% for the solid-boundary test at a RASJA height of 66cm, out of character from the other solid boundary profiles, and above the sand bed with a RASJA height of 71cm. These profiles show more consistency with height than we observed with the near-bed ADV measurements but show overall agreement.

3.3 Turbulence Intensity and Kinetic Energy

Turbulence intensity is typically a nondimensional quantity used to describe the level of turbulence in a flow, shown as the strength of velocity fluctuations

normalized by the mean velocity, such that

$$I = \frac{\sqrt{\overline{u'^2}}}{\overline{u}}$$

where u' denotes instantaneous fluctuating velocity and $\overline{u}$ denotes mean velocity. In the case at hand, in which mean flow is effectively zero, we would find an infinitely high turbulence intensity, which is of little physical significance. Thus, we must use an alternate approach. In this analysis, we use a dimensional turbulence intensity to qualitatively analyze the near-boundary flow structures. The average of u' approaches zero by definition, so instead we use the r.m.s. velocity and replace u' with u_f such that u_f describes a dimensional turbulence intensity:

$$I = u_f = \sqrt{\overline{u'^2}}$$

For the remainder of this chapter we will discuss I as a dimensional turbulence intensity which will be normalized in Chapter 5. Symmetry of the tank is assumed such that statistics in the x-direction are equal to statistics in the y-direction, or $u_f = v_f$ for these calculations. PIV data were used to calculate the horizontal and vertical turbulence intensities along vertical profiles above the bed, which assumes horizontal homogeneity due to geometric symmetry of the tank.

In addition to turbulence intensity that we consider in particular coordinate velocity directions, we can also compare turbulent kinetic energy as defined previously. However, accounting for horizontal homogeneity in the PIV measurements, we adapt the formula such that:

$$k = \overline{u'^2} + \frac{1}{2}\overline{w'^2}$$

3.3.1 Solid Boundary

With a solid glass boundary in place at the bottom of the tank, we examined the effect of changing the height of the suspended jet array on the resulting turbulent boundary layer. The RASJA height was varied in 5cm increments ranging from heights 71cm above the bed to 41cm above the bed. Variano and Cowen (2008) found that the jets may not be fully merged at a location less than 6 jet spacings away from the RASJA, and so with a 10cm distance between adjacent jets, any jet heights beneath 60cm may not result in the formation (or decay) of homogeneous near-isotropic turbulence. Thus the measurements made at the uppermost three RASJA heights are the most reliable, though all seven have been included for comparison.

Figure 3.9 shows the horizontal and vertical turbulent intensities calculated from the 10cm PIV FOV above the lateral center of the bed. There is a noticeable decay in vertical turbulence intensity and growth in horizontal turbulence intensity toward the bed. The horizontal turbulence intensity at the bed is zero because of the no-slip condition, and vertical turbulence intensity is zero due to the kinematic boundary condition.

The dimensional Figure 3.9 shows that altering the jet heights results in a similarly-shaped turbulence intensity profile, with more pronounced features as the jets approach the bed, diminishing the volume of the tank and the distance over which the homogeneous turbulence can decay near the bed. In the limit of

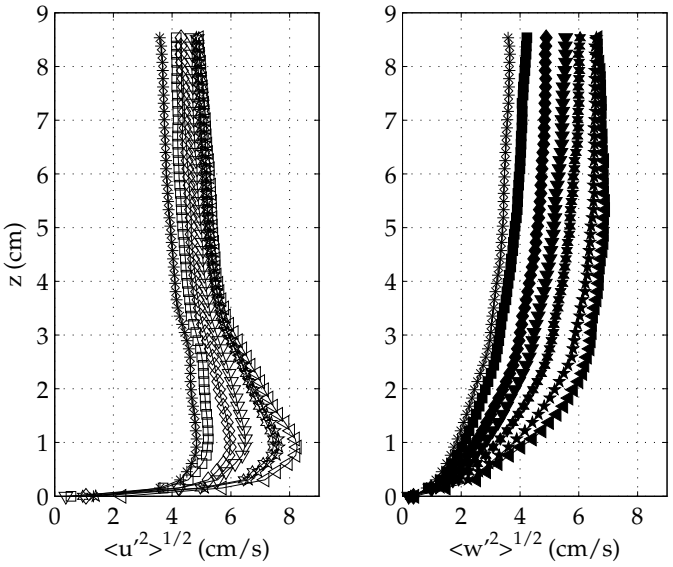

Figure 3.9: Turbulence Intensity above a flat impermeable boundary with varied jet heights

the distance between the bed and the jets approaching zero, we would have no jet-merging region and would lose homogeneity and isotropy, with significant splats and antisplats from active jets, not from mixed turbulence.

Figure 3.10 shows the turbulent kinetic energy profile above the boundary. The shape of the profile is greatly influenced by the shape of the horizontal velocity fluctuations, again showing double and single peaks towards the boundary. For the tests in which the jets were most elevated above the bed, the energy profile approaches a constant value, near $40\frac{cm^2}{s^2}$. Similarly to the horizontal turbulent intensity (Figure 3.9), there is a noticeable increase in the energy near the bed, approximately 3cm above the bed in this case.

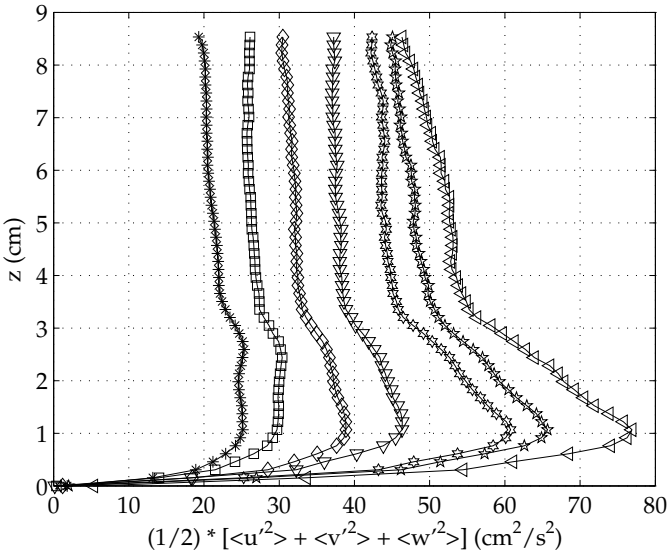

Figure 3.10: Turbulent Kinetic Energy above flat impermeable bed with varied jet heights

3.3.2 Sediment Boundary

The experiment was repeated with a sediment boundary to examine the turbulence intensity at the bed when the jets were raised to maximum height in the tank. During this trial, small resuspension events were observed on occasion, and minor bed deformations had begun to develop, as the jets had been running for 30 minutes prior to the recording of this PIV dataset. Still, the bed remained reasonably flat, particularly in the FOV over which measurements were made, as the center of the tank evolved more slowly than regions near walls. Thus, we may consider this boundary to be permeable and movable, but by no means was there significant sediment transport along the bed.

In Figure 3.11 we note a significantly diminished turbulence intensity enhancement effect within 3cm of the bed with a sediment boundary as compared to the solid boundary with the same jet height, as the porosity of the bed allows

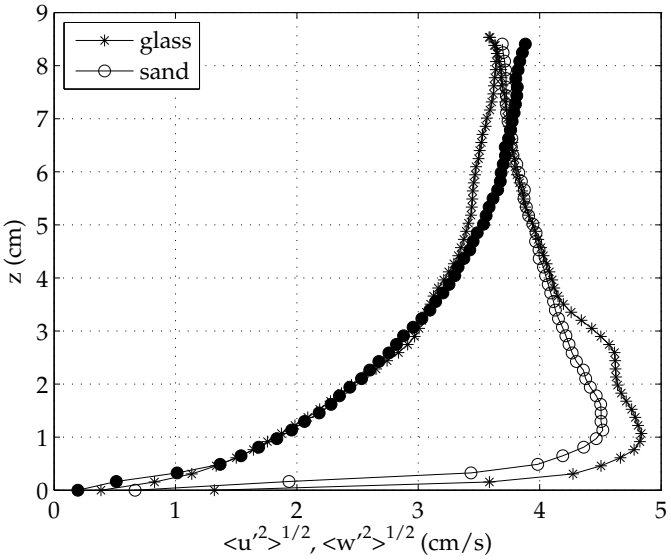

Figure 3.11: Turbulence Intensity comparison between sediment and solid boundary

vertical fluid motions to pass into the boundary instead of requiring a complete transfer of kinetic energy to the horizontal as occurred with the solid glass plate. The sediment is also capable of resuspending in this tank configuration, so energy of the flow can translate to sediment motion. The vertical turbulence intensity is nearly equal for the sediment and solid boundaries.

Considering the energy profile shown in Figure 3.12, the energy is relatively constant with height for the sediment boundary, compared to solid boundary energy profiles that abruptly increase near the bed. Above the boundary-influenced flow, defined as the region within 4cm of the bed, the energy of the flow is very similar for both sediment and solid boundaries. Again, this diminished energy between the solid and sediment boundaries can be accounted for as energy in the flow causes movement of sediment or a transmission of energy into the bed, where we are unable to capture data with the instruments available.

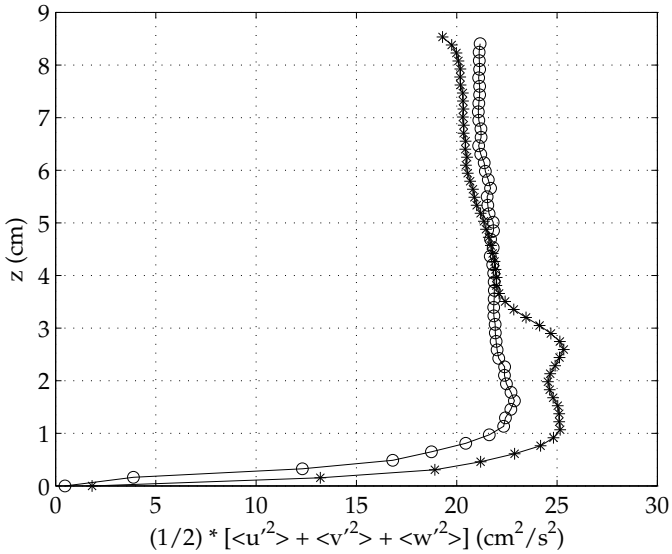

Figure 3.12: Turbulent Kinetic Energy comparison between solid and sediment boundary

3.3.3 Error Analysis

By performing a bootstrap analysis (Efron and Tibshirani, 1993) on the turbulence intensity, we can construct a 95% confidence interval for these profiles and determine whether our 30-minute averaged results are likely representative of the true turbulence intensity. Results are shown in Figures 3.13 and 3.14. The dash-dotted lines represent the 2.5% and 97.5% cutoff values in the bootstrap analysis, thus the range between shows the values within which the true turbulence intensities likely lie. In the bootstrap analysis, 1,000 samples were used. The computed average turbulence intensities indeed fall nearly central in these ranges with very low error.

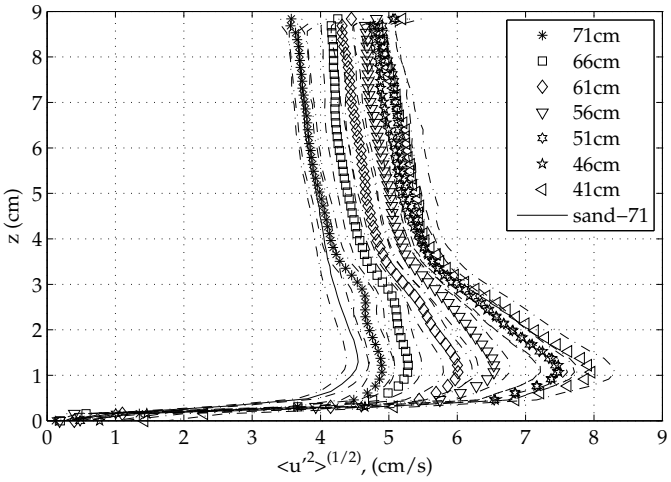

Figure 3.13: 95% Confidence Interval for Horizontal Turbulence Intensity from Bootstrap Analysis

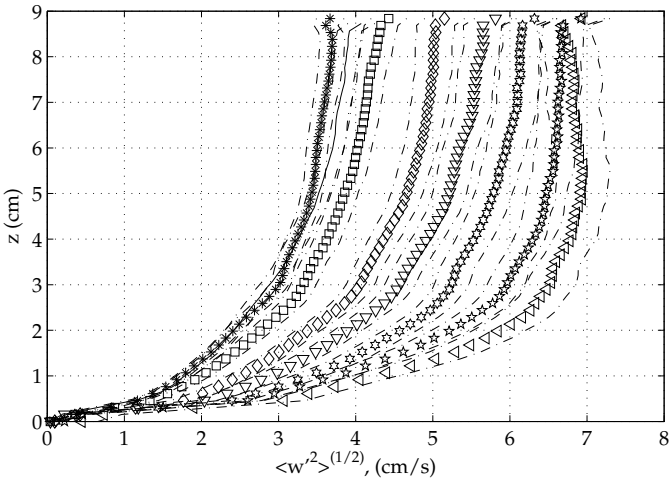

Figure 3.14: 95% Confidence Interval for Vertical Turbulence Intensity from Bootstrap Analysis

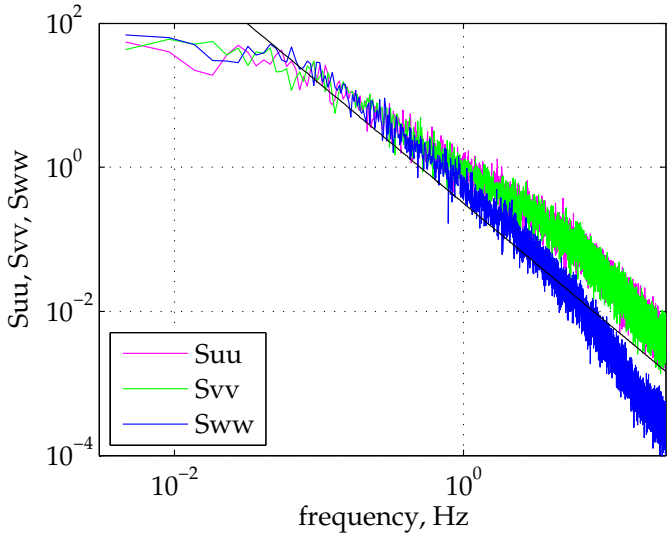

Figure 3.15: Temporal Spectra of velocity with 11 ensemble averages; 30 minute 50Hz ADV measurement at z/H=0.14

3.4 Temporal Spectra of ADV Measurements

With the ADV measurements recorded along the vertical depth of the tank above a glass bed with maximum jet height $H = 71cm$, we are able to compute temporal spectra of the horizontal and vertical velocities. In the spectra, we see a substantial intertial subrange with a slope of $-\frac{5}{3}$. An example of this is shown in 3.15, which shows excellent agreement between all three spectra and the standard -5/3 slope, despite slightly higher noise tails in both the u and v horizontal velocities than in the vertical velocity spectrum.

3.5 Dissipation

There are several methods through which we can compute dissipation rates from the PIV data. Computing the longitudinal structure function from the re-

sultant PIV velocity fields will produce an estimate for dissipation. Estimates for dissipation can also be found by analyzing spatial spectra according to Kolmogorov theory.

3.5.1 Structure Function Estimate

With the 10cm PIV FOV data, the structure function D_{LL} can be calculated (Pope, 2000). With an x location given as the center profile, and $\frac{r}{2}$ values ranging from zero (at $x = 0$) to 5 at the edge of the FOV, where r is the separation distance between data points, the following formula is used, with angle brackets denoting a temporal average.

$$D_{LL}(x, r) =< [U(x - \frac{r}{2}) - U(x + \frac{r}{2})]^2 >$$

Using the relationship between the structure function and dissipation, ε, with a constant $C_2 = 2.0$ from Pope (2000), we can solve for dissipation in regions where the structure function, a function of separation distance, becomes flat. With this function, the value of dissipation will be seen graphically as the asymptotic value that $\varepsilon(r)$ approaches, an example of which is shown in Figure 3.16.

$$D_{LL} = C_2(\varepsilon r)^{\frac{2}{3}}$$

$$\varepsilon = \frac{1}{r}\left(\frac{D_{LL}}{C_2}\right)^{\frac{3}{2}}$$

The resultant profiles of dissipation from the structure function can be summarized in Figure 3.17. The shapes of the profiles are very similar, regardless of

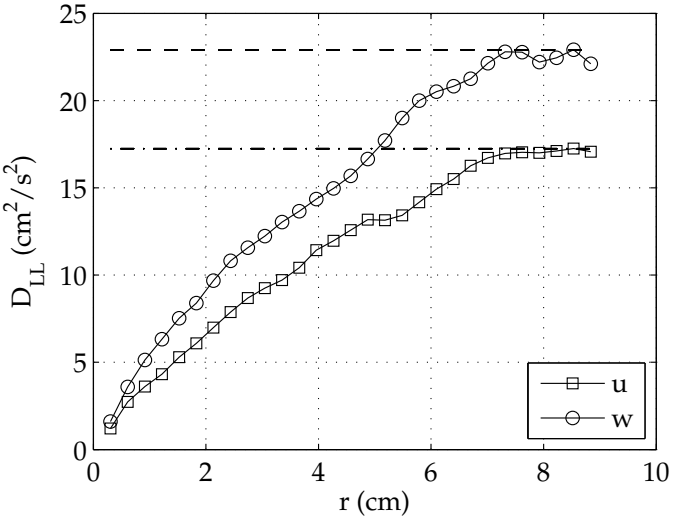

Figure 3.16: D_{LL} approximation; dissipation values shown by dashed lines

the bed material. The value of dissipation computed from vertical velocities increases with depth, whereas the dissipation profile from the horizontal velocity structure function increases dramatically near the bed, and decays with height. This is to be expected as the theory is based on homogenous isoptropic turbulence and the assumption of isotropy is strongly violated near the wall. Above the bed-influenced region, approximately 3cm above the bed, dissipation above a sediment bed is slightly greater than dissipation above a solid bed. This trend is reversed within the boundary-influenced region, though the two are quite close in magnitude.

3.5.2 Spatial Spectra Estimate

The following formula shows the relationship between spatial spectra and dissipation, with the constant $\alpha = 1.5$ and wavenumber k_1.

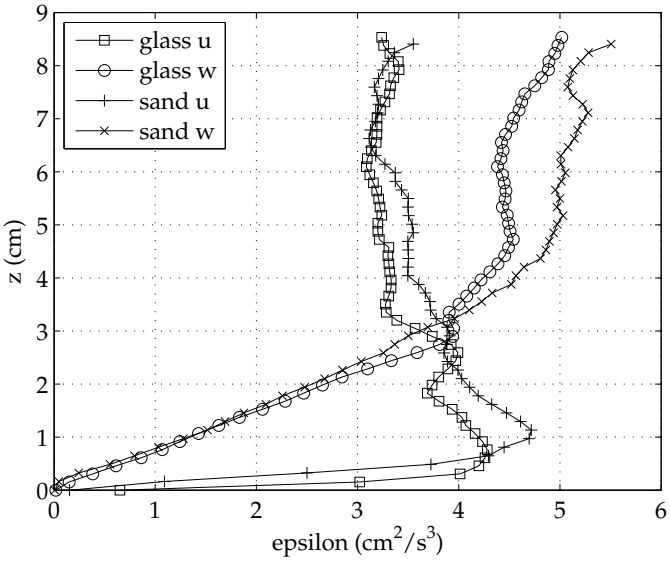

Figure 3.17: Dissipation profiles computed from 2nd order structure function

$$S_{uu}(k_1) = \frac{9}{55}\alpha\varepsilon^{\frac{2}{3}}k_1^{\frac{-5}{3}}$$

$$\varepsilon = (\frac{9}{55\alpha}S_{uu}(k_1)k_1^{\frac{5}{3}})^{\frac{3}{2}}$$

Figure 3.18 shows the results of this analysis using the spatial spectra computed from the horizontal and vertical velocity records with the PIV data at a given elevation (Pope, 2000). The relationship between spectra for horizontal and vertical velocity records in assumed isotropic turbulence has a $\frac{3}{4}$ relationship, as:

$$S_{uu} = \frac{3}{4}S_{ww}$$

$$\varepsilon = (\frac{9}{55\alpha}\frac{3}{4}S_{ww}(k_1)k_1^{\frac{5}{3}})^{\frac{3}{2}}$$

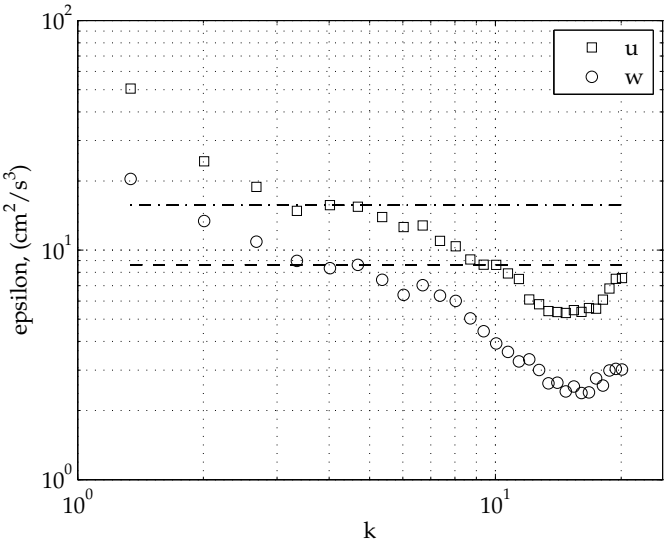

Figure 3.18: Dissipation estimate approximately 3cm above a sand bed

Computing dissipation with the spatial spectra, we see different results than when computing dissipation from the 2nd order structure function. The resulting profiles are summarized for comparison in Figure 3.19. The shapes of the profiles from vertical velocities are similar to each other, and the profiles from horizontal velocities are distinctly similar to each other and different from the vertical, again as expected due to the violation of the assumption of isotropy. However, unlike the profiles computed from the structure function, overall the sediment dissipation is greater than the dissipation above a solid bed. The profiles still cross near a height above the bed at z=3cm, near the apparently bed-influenced region, as is consistent with the other dissipation profiles. Dissipation magnitudes of 10-15 $\frac{cm^2}{s^3}$ seem quite different from magnitudes of 3-5 $\frac{cm^2}{s^3}$ between the two methods of computing dissipation; however; this is a very difficult measurement to make with certainty.

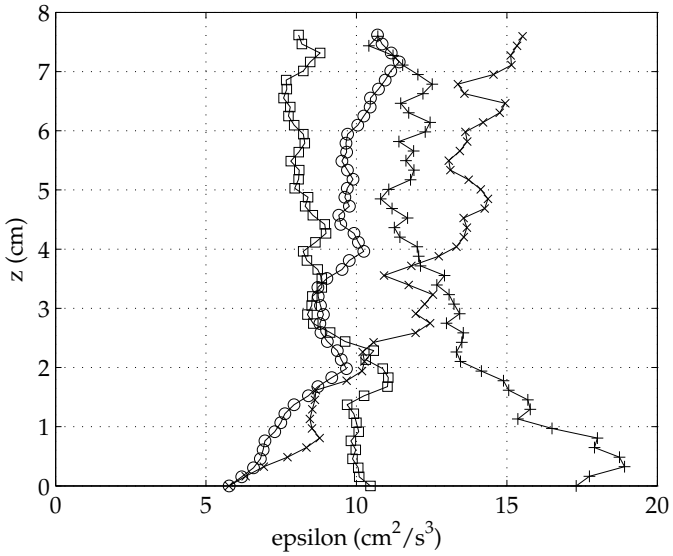

Figure 3.19: Dissipation profiles computed from spatial spectra

3.6 Turbulent Length Scales

3.6.1 Integral Length Scale from Autocorrelation Function

In order to better understand the length scales associated with the various conditions of turbulence present in the tank, comparisons of the integral length scales were computed according to an autocorrelation function presented in Variano and Cowen (2008). For the profiles shown, the RASJA was suspended above the tank at H=71cm, so that direct comparisons between solid and sediment boundaries can be made. The autocorrelation function is defined as:

$$a(r) = \frac{\overline{u'(x - \frac{1}{2}r) * u'(x + \frac{1}{2}r)}}{\overline{(u'(x - \frac{1}{2}r)^2} * \overline{u'(x + \frac{1}{2}r)^2)}^{\frac{1}{2}}}$$

An example of the autocorrelation function is shown in Figure 3.20. This particular curve is taken approximately 7cm above the sediment bed. The data for

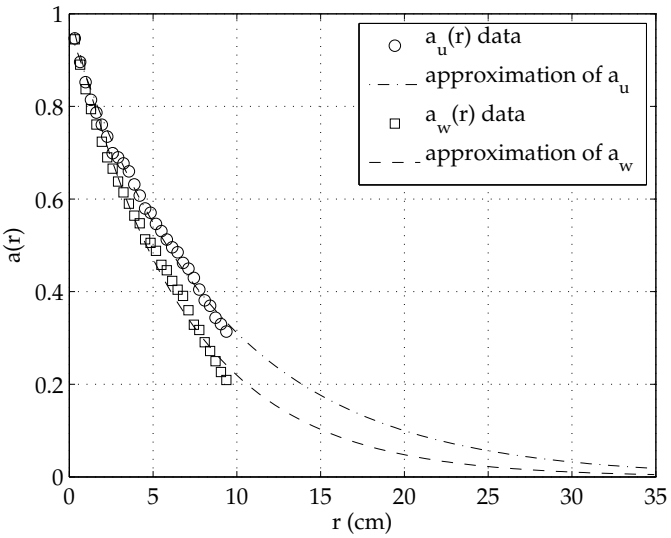

Figure 3.20: Autocorrelation function extrapolation sample for sand bed, 7cm above bed

the horizontal and vertical velocity autocorrelations is shown by the circle and square points. With a FOV of only 9cm, we cannot capture the entire autocorrelation function approaching zero, so an exponential extrapolation has been performed out to approximately 35cm, where the curves approach zero. With the extrapolation beyond a smaller FOV, error is introduced, but the results show smooth profiles and fair agreement with Variano's analysis, where he was able to measure a 40 cm FOV and hence did not have to interpolate, sufficient for an approximation of the integral length scale with the given datasets.

From an autocorrelation function computed at each height in the FOV, the integral length scale can be computed by simply taking the integral of the exponential extrapolation, according to:

$$L = \int a(r)\, dr$$

The resulting profile of the integral length scale computed from the horizontal

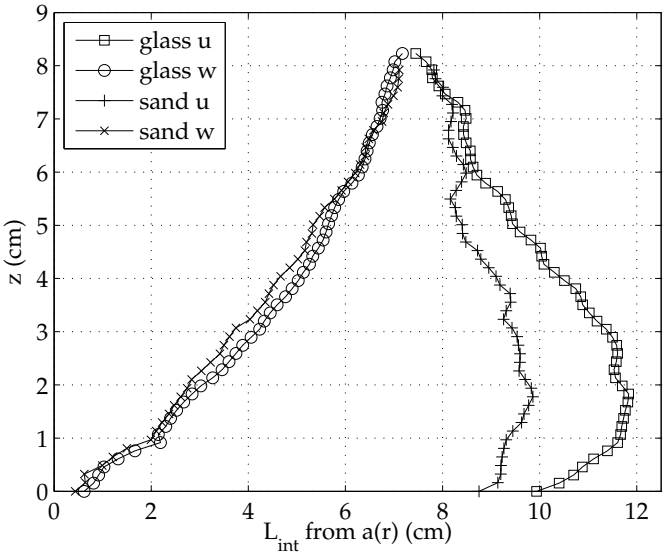

Figure 3.21: Integral Length Scale computed from autocorrelation function above solid and sediment beds

and vertical velocity autocorrelation profiles is shown in Figure 3.21. The resulting profiles are quite similar after changing the bottom boundary conditions, but the integral length scale profiles are different when calculated from the vertical or horizontal velocity autocorrelation functions. Above a glass boundary, the integral length scale approaches values of 7.4cm and 7.2cm toward the top of the FOV, computed from the horizontal and vertical velocities, respectively, and 7.8cm and 7.1cm above a sediment boundary.

3.6.2 Kolmogorov and Taylor Microscales

From Pope (2000) we can find the length and time scales of the smallest turbulent eddies. Through scaling, we have the relationships

$$\eta = (\frac{\nu^3}{\varepsilon})^{\frac{1}{4}}$$

$$\tau = (\frac{\nu}{\varepsilon})^{\frac{1}{2}}$$

As part of the characterization of the turbulence facility, we compute η=0.022cm, and τ=0.050s above a glass bed. We can also examine the turbulence Reynolds number as:

$$Re_L = \frac{k^2}{\varepsilon\nu}$$

where L denotes the integral length scale and k denotes turbulent kinetic energy. From these calculations, we find a rather high Re_L=12,050. The Taylor-microscale Reynolds number, which is applicable to grid turbulence with assumed isotropy, is defined as:

$$Re_\lambda = \frac{u'\lambda_g}{\nu} = (\frac{20}{3}Re_L)^{\frac{1}{2}}$$

with

$$\lambda_g = \sqrt{10}\eta^{\frac{2}{3}}L^{\frac{1}{3}}$$

We find the Taylor-microscale Reynolds number to be 283, similar to 314 found in Variano and Cowen (2008), and λ_g of 0.49cm, an intermediate length scale between the smallest and largest turbulent eddies.

CHAPTER 4

SIMULTANEOUS AQUADOPP HR PROFILER AND PIV MEASUREMENTS ABOVE A SEDIMENT BOUNDARY

As a side project in the thesis work, there was an opportunity to study the performance of an acoustic current profiler to evaluate its performance in a highly turbulent flow. The Aquadopp High Resolution Profiler is designed to capture velocity measurements in the field, typically in flows with fairly large physical scales. Due to the design of the instrument, it struggles to capture accurate data in energetic flows with very small turbulent structures, such as those near boundaries. We investigate the performance of the HR Profiler in the turbulence tank, and compare data with simultaneous PIV measurements to judge its accuracy and to determine the best way to use the instrument in order to capture relevant flow statistics for turbulence analysis. All tests were performed above a sediment bed.

4.1 Instrument Considerations in Data Analysis

4.1.1 Phase-wrapping

Using the Aquadopp HR Profiler with its minimum sample volume of 7mm and blanking distance of 10cm, the maximum velocity range was limited to +/-13cm/s. During data collection, there was a concern with phase-wrapping. Phase-wrapping occurs when the actual flow velocity exceeds the instrument velocity range. Consequently, the value wraps around, such that a reading of 15cm/s, exceeding the +/-13cm/s limit, will be recorded as -11cm/s. Initially,

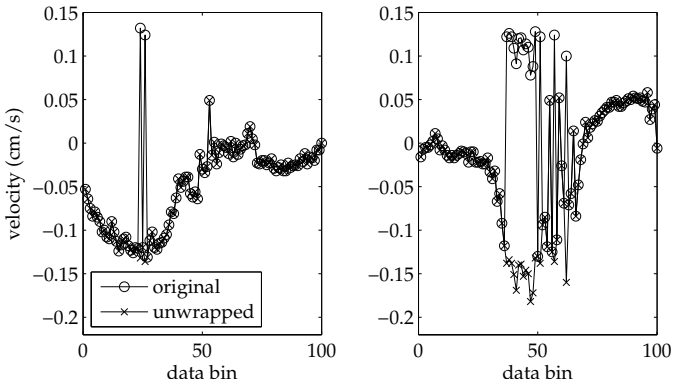

Figure 4.1: Phase-wrapped and unwrapped velocity data

the phase-wrapping did not appear to be significant, so the "extended velocity range" option was not selected during experiments. After viewing the data, it was realized that nearly 20% of the velocity files showed phase-wrapped data. With these particular datasets, the data was manually unwrapped by visually inspecting each file and correcting the datapoints. Figure 4.1 shows two examples of this phase-wrapping and the subsequent unwrapping of the files.

The effect of phase-wrapping on mean velocity is shown in Figure 4.2. This particular example comes from a beam velocity dataset for the upward-looking Profiler. The typical error between the mean velocity for phase-wrapped and unwrapped data is approximately 0.3cm/s, which shows an absolute error of 2% as considered over the 26 cm/s total velocity range. Compared to a mean velocity of 0cm/s, however, this causes a significant discrepancy.

We can also look at the temporal spectra of the velocity data before and after removing the phase-wrapping. In Figure 4.3, it can be noted that upon correcting the data, the magnitude of the spectrum increases slightly, maintaining nearly the same shape and slope of approximately -5/3, as expected in turbulent flows. We are thus inserting the energetic events back into the flow by

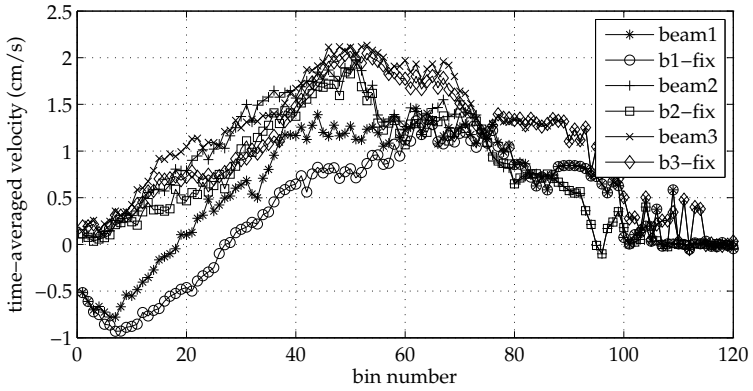

Figure 4.2: Phase-wrapped and unwrapped mean velocity profiles

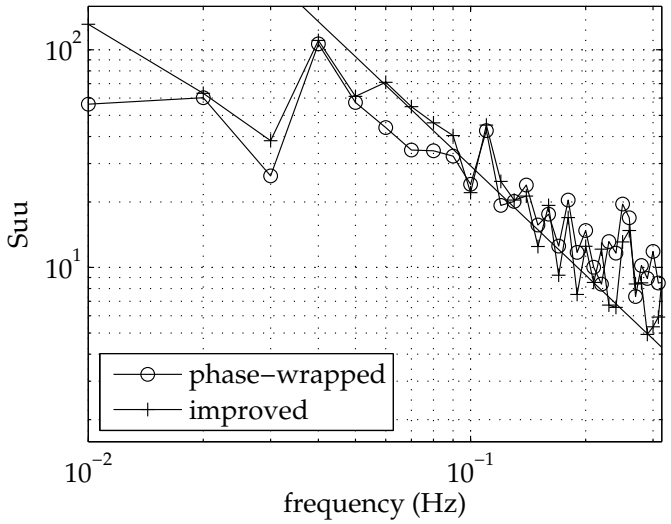

Figure 4.3: Phase-wrapped and unwrapped spectra comparison

unwrapping the data.

This discrepancy seen in the spectra can also be observered in plots of the variance, as shown in Figure 4.4. Here, we note a 20% increase in variance after removing phase-wrapping. The downward spike in the beam 1 velocity record shows the location at which the beam hit a glass sidewall and continued to record along the reflection from the wall through the remaining height of the tank. After considering the differences in the spectra and variance before and

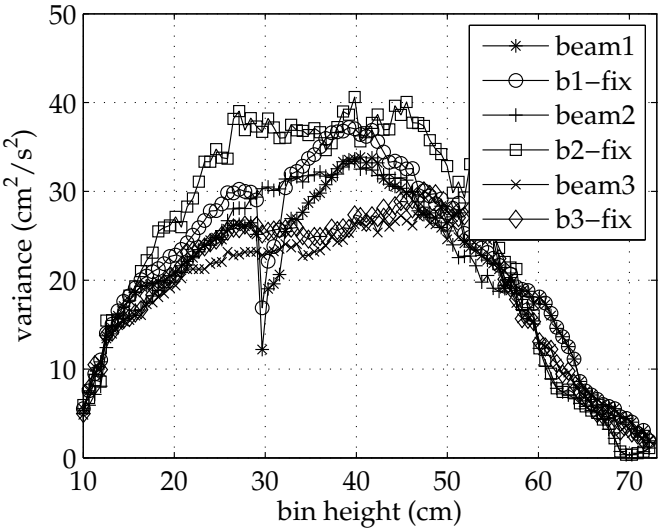

Figure 4.4: Phase-wrapped and unwrapped variance comparison

after removing phase-wrapping, it is evident that energy is lost in the data analysis if we neglect to screen the data for this particular source of measurement error.

4.1.2 Boundary detection

The Aquadopp HR Profiler does not have a built-in distance measuring tool, as is customary in many other acoustic insruments. The instrument records data along the entire user-inputted length, even if that length exceeds the distance to the boundary. Measurements recorded beyond this length can be a combination of measurements through a permeable boundary and reflections off of the boundary itself. These velocity readings are thus not reliable measurements, and the amplitude and correlation files must be analyzed to detect the sample bin in which the boundary is located. Figure 4.5 is an example of the amplitude and correlation files, and shows the point selected as the boundary location,

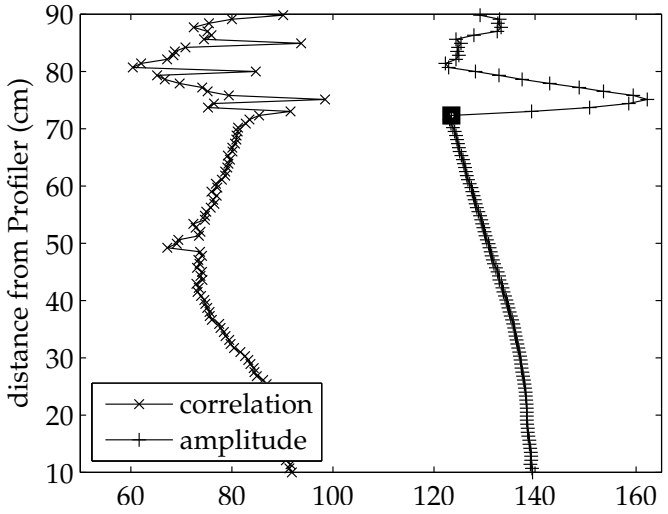

Figure 4.5: Amplitude and Correlation profiles to identify boundary

represented by the bold square on the amplitude profile.

An advantage of using instantaneous amplitude and correlation files to identify the boundary location is in the ability to detect a moving boundary during velocity recordings. With the method used, only boundary movements greater than the 7mm sample volume could be detected, which was not the case in these particular experiments that had smaller bed deformation. Using curve fits of the amplitude files, smaller bed movements may be detectable. These may be of particular interest in field experiments in which it is useful to know the instantaneous boundary location with the true near-bed velocity measurements in the sample bins directly adjacent to the bed.

4.2 Velocity Measurements

In order to determine which HR Profiler measurements would best capture turbulent flow statistics, velocity measurements were made using both beam and

three-component velocity settings. The three experiments described consider vertical velocities measured along a single beam, beam velocity comparisons to PIV data, and three-component velocity comparisons to spatial PIV data.

4.2.1 Vertical Beam Velocity Measurements

Considering Figure 4.6 (in which negative velocities denote upward flow), we see mean vertical velocity profiles through the center of the tank, averaged over 30-minute records with 1Hz sampling. A trend can be observed as the height of the RASJA is altered in each of the seven tests, in that we notice a mean upward return flow of up to 3 cm/s in the jet-merging region when the jets are at their maximum height of H=71cm. Even though the jet firing pattern is identical for each of the 7 tests, we see different initial velocities even at the uppermost measurement bins, located nearly 4cm from the jet orifice plane. Since this measurement column is not located directly beneath a jet, but rather at the center of four jets, it follows that there would be a local return flow to continue to feed the jets; it is surprising that this upward flow extends through nearly the entire vertical column for the tests with the greatest jet heights, with a small upward flow immediately above the bed. As the RASJA approaches the bed, we see return flows with diminished magnitudes, and we see a flow reversal with the lower four jet heights. In these tests, we also have rapid bed deformation because there is less room for the turbulence to decay, so we note elevated energy near the bed and thus more energetic sediment resuspension. The jets have not necessarily merged, and they can directly impinge upon the bed. The enhanced bed activity and formation of vertical peaks (discussed in Chapter 6) is in agreement with the upward flows we see at the jet heights below 56cm.

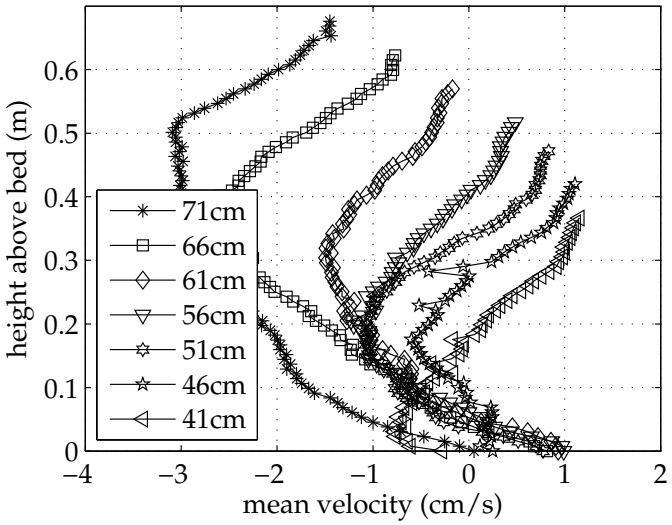

Figure 4.6: Vertical velocity profiles of Aquadopp HR Profiler with various jet heights

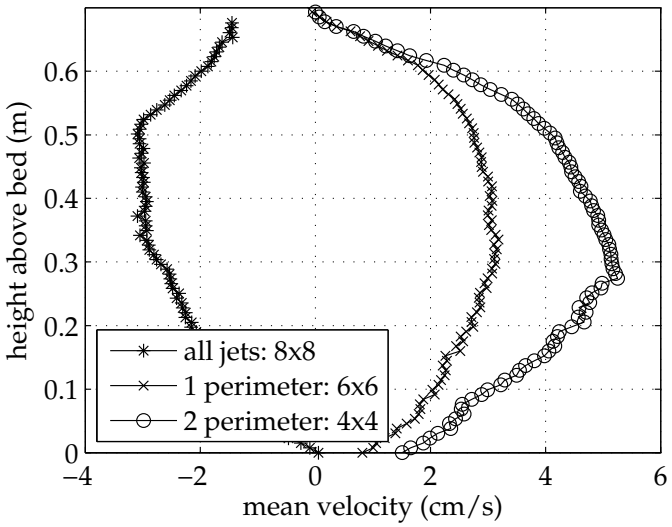

Figure 4.7: Vertical velocity profiles of Aquadopp HR Profiler with altered RASJA

In continuing to examine the role of the side boundaries on the energetics of the turbulence, the mean velocity profiles in Figure 4.7 are the result of turning off the outermost perimeters of the 8x8 array of jets, compared to the default 8x8 firing condition. The jet heights for each of these three tests is at the uppermost H=71cm. The most notable difference in these profiles is the direction of the flow. Instead of the upward return flow seen in the default firing state, we now observe a net downward flow through the center of the tank for both cases in which outermost jets were turned off. As expected, without the outermost jets firing, we have set up a toroidal flow in which the upward return flows are located along the un-forced side walls. As the active grid diminishes from a 6x6 to 4x4 jet array, this return flow is enhanced, as a very small region of the tank is responsible for the turbulence forcing. Overall, the 4x4 array acts as a single jet with downward momentum in the center of the tank with a large region for surrounding return flows. The implications of this will be further discussed in Chapter 6, as the impact of specific flow conditions on sediment resuspension and bed morphology is explored.

4.2.2 Beam Velocity Comparison

With the Aquadopp HR Profiler buried in the sand such that one beam passes through the PIV FOV, a direct comparison of velocity and statistical metrics of the flow can be made, after performing a coordinate transform on the PIV data to align the velocity readings along the 25 degree (from vertical) angle of the Profiler beam. We expect good agreement between these measurements, and indeed see in Figure 4.8 that the PIV and Profiler velocity measurements are very similar.

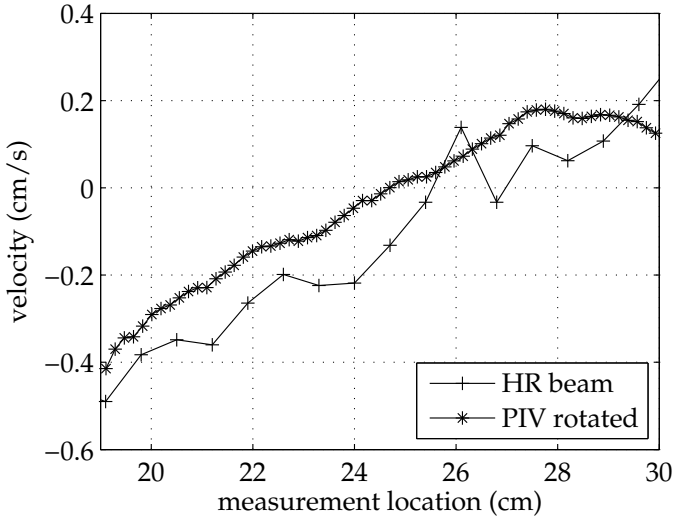

Figure 4.8: Beam and PIV velocity profile comparison

Even though we see good agreement between the PIV and Aquadopp HR Profiler velocity readings measuring in beam velocity, looking at the comparison of the variance of the velocity signal shown in Figure 4.9, we see that the variance of the HR Profiler data is nearly twice that of the PIV analysis. Both profiles show a consistent upward trend, but there is a notable quantitative error in the case of the HR Profiler, as is expected.

If we compare the temporal spectra computed from the PIV and Aquadopp HR Profiler data, as shown in Figure 4.10, there is further evidence of this error, due to background noise of the Profiler. Spectra were computed at nearly identical locations in the flow, and they are similar to spectra computed at other regions within the FOV. The magnitude of the spectrum computed with the Profiler is elevated above the spectrum of the PIV data fairly consistently by a factor of three, which shows evidence of a fairly constant noise floor of the instrument. Both show good agreement with the -5/3 slope, with minor noise tails.

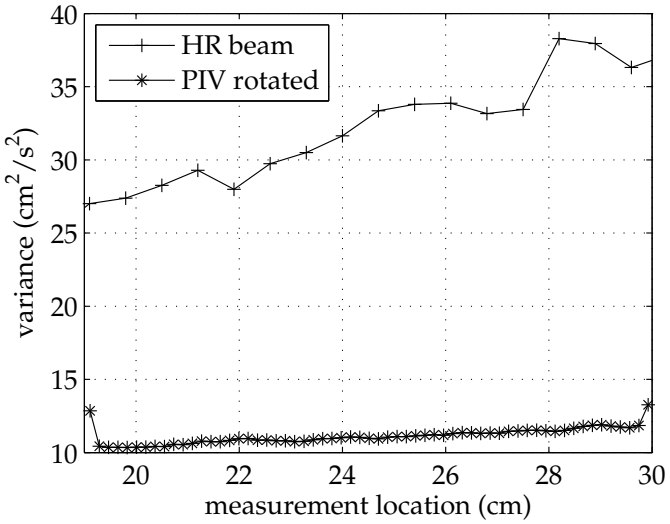

Figure 4.9: Beam and PIV variance profile comparison

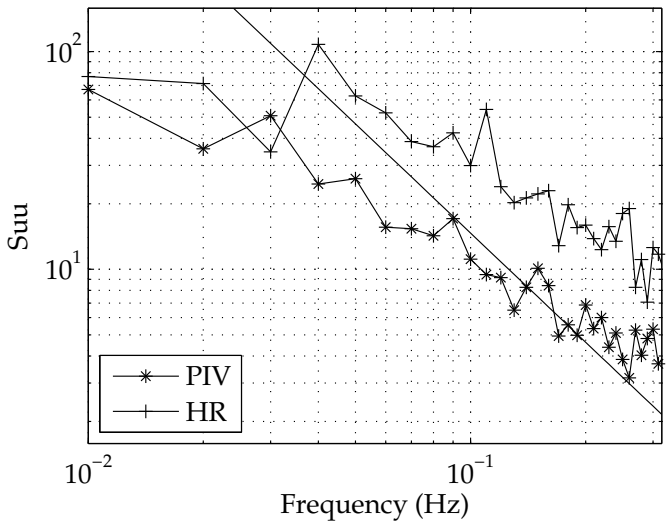

Figure 4.10: Beam and PIV sample spectra comparison

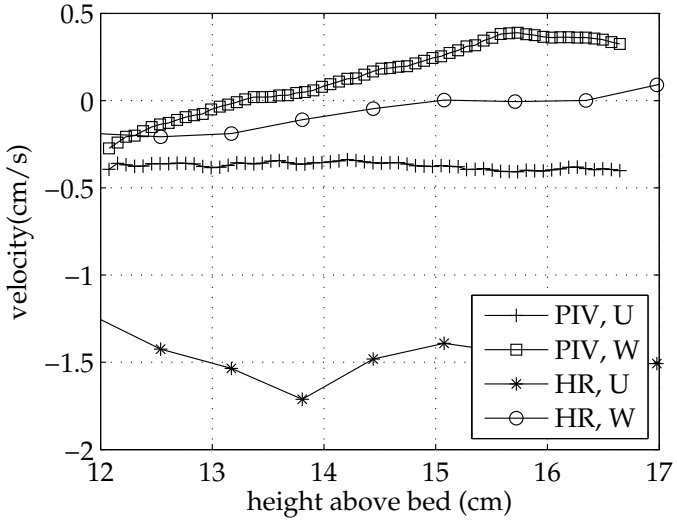

Figure 4.11: Aquadopp HR Profiler and PIV profiles of u, w.

4.2.3 Post-processed Velocity Comparison

The three recorded beam velocities on the Aquadopp HR Profiler were transformed into horizontal (u) and vertical (w) velocities that corresponded with the PIV velocities using a transform matrix in the header file of each HR Profiler dataset. The results are shown in Figure 4.11. At this height in the flow, in the range of 12-17cm above the HR Profiler, the beams have already spread approximately 14cm from each other. This is much greater than the integral length scale of the facility, which is approximately 7.8cm. Even though the individual beams may be capturing data from different individual turbulent events, we are interested in the statistics of the flow averaged over long periods of time. Figure 4.11 shows surprisingly good agreement between the HR Profiler and PIV data, with very similar results in the vertical velocity, but with greater error in the horizontal velocity measurement.

We can also consider the variance of the horizontal and vertical velocities, as

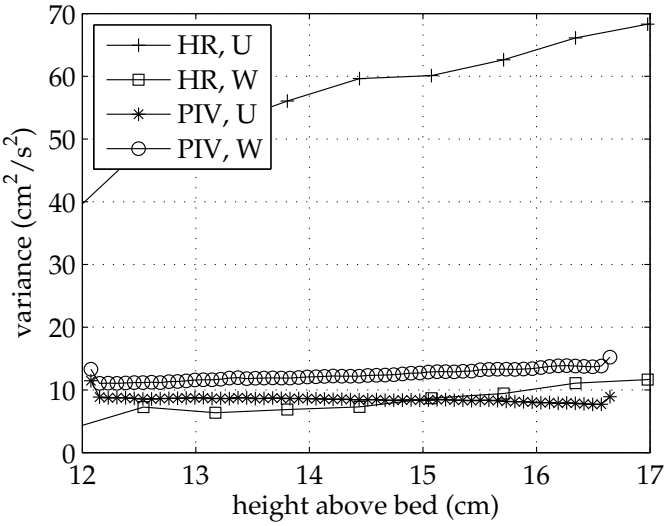

Figure 4.12: Variance of u, w from HR Profiler and PIV

shown in Figure 4.12. Here we see agreement in the vertical, as we saw with the direct velocity measurement, and disagreement in the horizontal velocity variance with the HR Profiler greater than variance of the PIV data by a factor of 5 due to the Profiler geometry.

4.3 Quantification of Turbulence Measurements

Analyzing the results from the Aquadopp HR Profiler, considering the effects of phase-wrapping and the direct comparison with fairly robust simultaneous PIV data, we can draw several conclusions about the use of the HR Profiler in this turbulence facility. The instrument is designed to capture metrics of much larger-scaled flows, such as uniform shear flows or field-scale turbulent flows. By using the instrument in a facility with side walls only 82cm in length, the instrument was truly not in its design flow. Yet several promising results were achieved as we gained a greater understanding of the potential and limitations

of the device in such flows.

Considering the effects of phase-wrapping, we saw an increase in the variance by approximately 20% after unwrapping the data that was affected by the extreme turbulent events and a slight increase in the temporal spectra as we recaptured energy lost in the extreme turbulent flow events. Had an extended velocity range been selected, or an alteration of the sample volume or other input parameters on the instrument been made, a greater velocity range would have diminished the prevalence of phase-wrapped data files. However, in such a confined laboratory space, we were aiming to ahieve the highest resolution measurements possible, and thus handled the phase-wrapping concerns following data collection. With this difference in mind, we saw a very significant noise floor of the instrument overall, regardless of the phase-wrapping error, when temporal spectra were compared between the Profiler and PIV analysis. The Profiler showed good agreement with expectations of turbulence and knowledge of the flow in this particular facility.

In using the instrument with several different mounting configurations, we had the advantage of using two different measurement techniques, comparing directly measured beam velocities to equivalent u, v, w velocity measurements along a single profile, computed from the instrument's transformation matrix. The beam velocity comparisons were, as expected, very reliably in agreement with PIV data. In the range selected, approximately 12-17cm from the instrument head, we also saw fair agreement between the u and w velocities, though the discrepancy in the horizontal velocity, due likely to the spatial spreading of the three measurement beams, showed that the instrument struggled to capture identical flow phenomena across all three beams simultaneously, as this facility

was a bit small for the instrument. Had the beams spread further for additional PIV comparisons, it is unlikely that strong agreement in the velocity measurements would have been observed when considering three-component velocity profiles. Though reliable measurements in the turbulent swash zone have been recorded they must be made with care, as downward-facing Profiler measurements may result in uncorrelated data, if the three beams have spread beyond the size of smaller near-bed turbulent length scales.

CHAPTER 5

BOUNDARY LAYER PROFILES

5.1 Bed Stresses and Friction Velocity Theory

When considering boundary layer characterization, one of the important features to consider is the determination of bed stress. In this facility, we want to deduce the resultant stresses when decaying homogeneous isotropic turbulence interacts with a solid glass or sediment boundary. We aim to understand the resulting stress during resuspension events to determine the requisite critical fluid stresses for incipient particle motion from a stationary bed, and during bed morphology episodes to understand the role of stresses with bed deformation.

Starting with the Reynolds Averaged Navier Stokes (RANS) equations, assuming no mean velocity in any direction and no gradients in the horizontal coordinate directions, we are left with the following equations for horizontal and vertical fluid momentum:

$$\frac{d\overline{u'w'}}{dz} = 0$$

$$\frac{d\overline{w'w'}}{dz} = 0$$

Using the no slip condition, which would imply zero Reynolds stress at the bed, this condition of no vertical gradients of the averaged Reynolds stress suggests that when averaged across a significant period of time, there are no Reynolds stresses throughout the tank, as shown in Figure 5.1. However, due to evidence

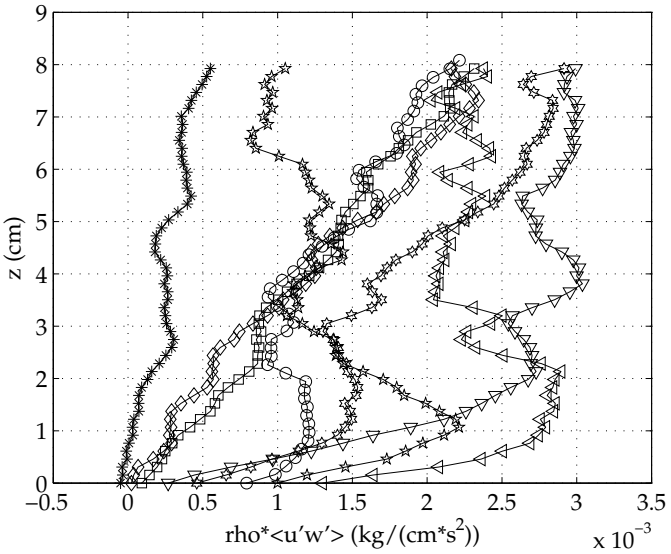

Figure 5.1: Temporally Averaged Reynolds Stress

that stresses exist, as the forced tank turbulence is capable of suspending sediment at intermittent time periods, we know that this is not the case, and so surely we must consider an alternate method of averaging to ensure that local stresses due to the Reynolds stress are kept intact statistically.

If we return to the traditional channel flow definition of stress, keeping both viscous and Reynolds stress components, we can attempt to use this formulation to calculate wall stress.

$$\tau_w = \mu \frac{d\overline{u}}{dz} - \rho \overline{u'w'}$$

Furthermore, friction velocity u_* can be determined from the wall stress, according to its formal definition, as:

$$u_* = \sqrt{\tau_w / \rho}$$

Once we establish a proper formulation for bed stress, we will be able to parameterize shear stress into an appropriate threshold u_* for sediment resuspension

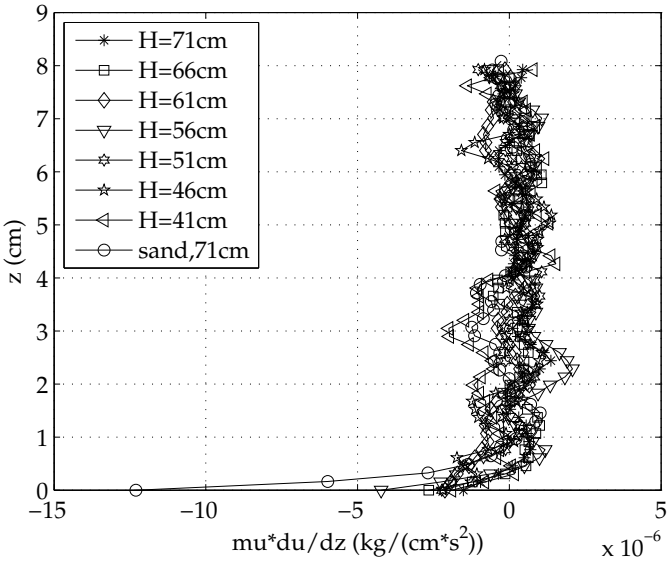

Figure 5.2: Viscous stress calculation for uppermost jet height, comparing solid and sediment boundary conditions

in a highly turbulent environment absent mean shear.

Again, considering the no-slip condition, which requires that the Reynolds stress term is equal to zero at the bed and that wall stress is equal to the viscous stress, we are left with a wall stress equation that does not apply to the experimental facility, as we have negligible mean flow and, again, no wall stress, which we know is not the condition in a facility in which bed deformation and sediment resuspension is apparent. In order to confirm that there is negligible viscous stress in the facility, profiles shown in Figure 5.2 were computed. Viscous stress was calculated locally using a finite difference method, and the resulting stresses were averaged horizontally across the FOV and in time, such that local velocities were considered instead of the bulk 30-minute average velocity $\overline{u} = 0$. Indeed, Figure 5.2 shows a resultant viscous stress of approximately zero, even within millimeters of the bed.

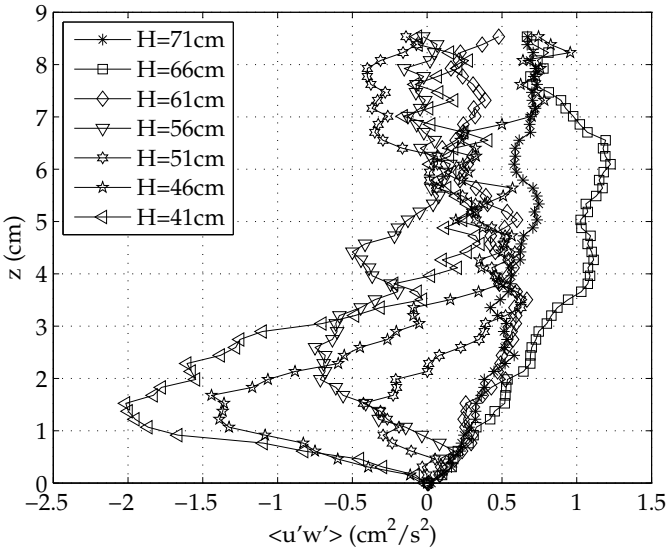

Figure 5.3: Profile of $\overline{u'w'}$

5.2 Quadrant Analysis and Reynolds Stress Profiles

To evaluate Reynolds stresses, we can compute a simple temporal average over the product of all velocity fluctuations, and then average horizontally across the FOV in order to produce a resulting profile, as shown in Figure 5.3 and Figure 5.4. The profiles in Figure 5.4 are consistent with the turbulence intensity profiles presented in Chapter 3, as the turbulence intensity is simply the square root of the normal Reynolds stresses.

In this particular flow, we expect $\overline{u'w'}$ to approach zero. The resultant profile is not identically zero, but it is clearly less organized than the other Reynolds stress profiles. An alternate method of taking this average is simply to take the absolute value of each Reynolds stress term prior to temporal and spatial averaging. This results in Figure 5.5, which is more consistent with the magnitudes and shapes of Figure 5.4.

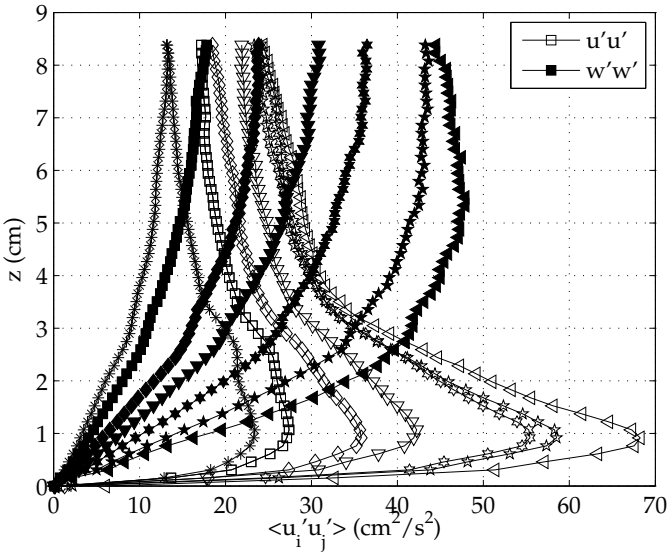

Figure 5.4: Profile of normal Reynolds stresses $\overline{u'u'}$, $\overline{w'w'}$

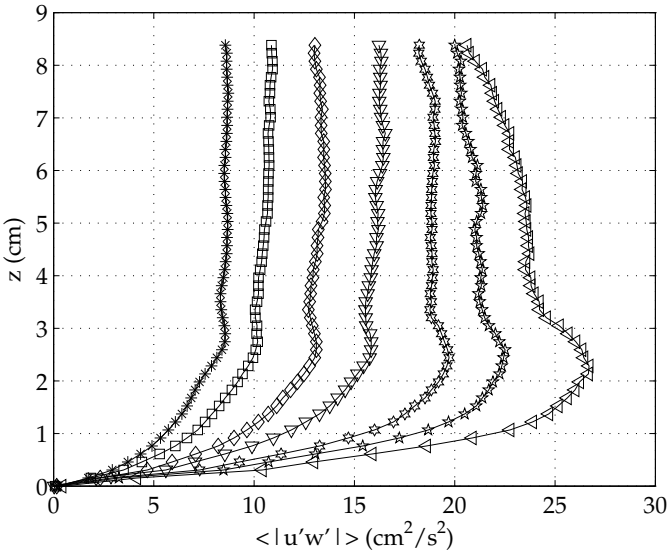

Figure 5.5: Profile of $\overline{|u'w'|}$

Another approach to a Reynolds stress analysis is to consider scatterplots and visualize velocity fluctuations present through a conditional quadrant analysis of the PIV dataset. By performing quadrant comparisons, we can examine the Reynolds stresses and make judgments regarding typical correlations of velocity fluctuations in boundary-influenced regions of the flow, typically within a few centimeters of the bed. In addition to plotting a traditional scatterplot shown in Figure 5.6, in which the x-axis represents horizontal velocity fluctuations, and the y-axis represents vertical velocity fluctuations, such that Quadrant I contains data points with upward and rightward velocities, Quadrant II countains points with leftward horizontal fluctuations and positive vertical fluctuations, etc., Figure 5.8 compiles this quadrant data into profiles that show the resulting $\overline{u'w'}$ structures that prevail in each of the four quadrants, and Figure 5.5 shows the absolute value of each of the 4 quadrant profiles at varying RASJA heights, averaged in time and horizontally across the FOV according to the number of velocity records in each quadrant. Figure 5.10 directly compares the Reynolds stress profiles above sand and sediment beds, each with a RASJA height $H = 71cm$ after performing a weighted average of the quadrant profiles, according to the population of Reynolds stresses in each quadrant. Finally, Figure 5.11 shows a comparison between the two different averaging schemes, using either the weighted quadrant average or an average of the absolute values of the Reynolds stresses. The profiles are shaped quite similarly, and have a consistent trend with decreasing jet height. Features such as bumps in the profile that denote the bed-influenced region occur at comparable heights. In general, the quadrant average is slightly greater in magnitude than the absolute value average. The discrepancy between the two profiles increases consistently with measurement distance above the bed.

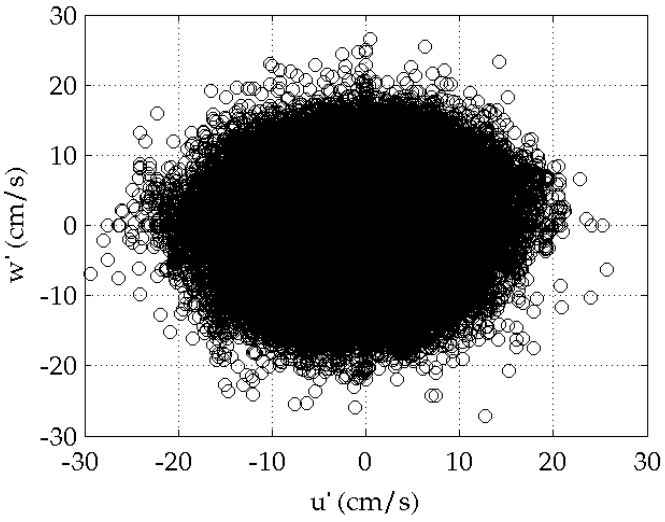

Figure 5.6: Scatterplot of all sand data velocity fluctuations

If we further consider the quadrant analysis, we can view the relative prevalence of fluid motion events to fall into each of the four quadrants to better understand the structure of the scatterplot shown in Figure 5.6. Figure 5.7 shows a sample breakdown of this, taken at a representative jet height of H=71cm. In an ideal homogeneous isotropic turbulent flow, we would expect each of the four profiles to fall along 25% with fluctuations equally likely to be leftward/rightward or upward/downward. However, along the bed, we do not see precisely this. Instead, we noticed that very near the bed, Quadrants I and II are significantly more populated, as they contain the upward vertical velocity fluctuations, or upward ejections from the bed. Quadrants I and III and Quadrants II and IV are nearly symmetric about 25%, crossing at heights in the FOV of approximately 0.3cm and 0.7cm, respectively. Thus above these two heights, we see that Quadrants III and IV are more highly populated than Quadrants I and II, and downward flow is more likely.

The weighted average $\overline{u'w'}$ plot in Figure 5.9 shows a similar trend to the $\overline{u'u'}$

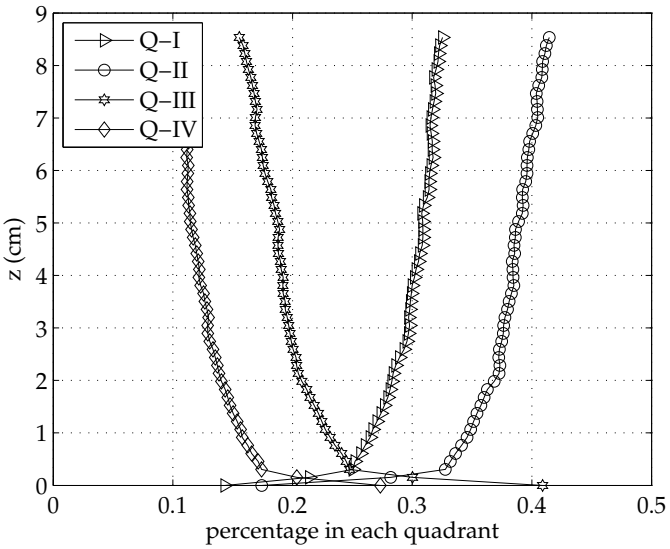

Figure 5.7: Percentage of data in each quadrant above glass bed, H=71cm

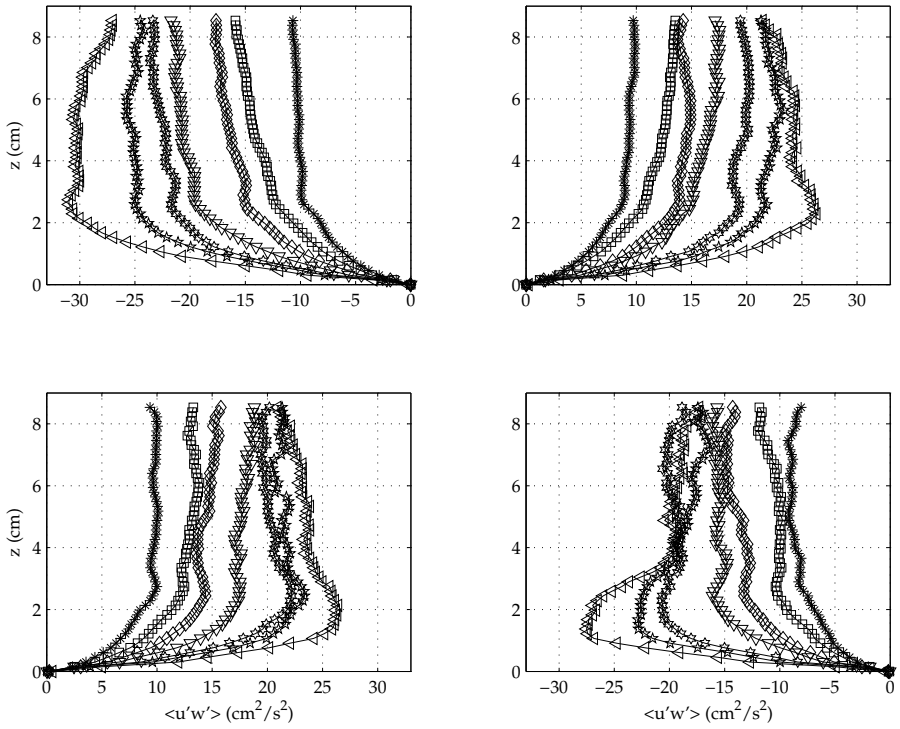

Figure 5.8: Quadrant Reynolds Stresses, counterclockwise from top right (I, II, III, IV)

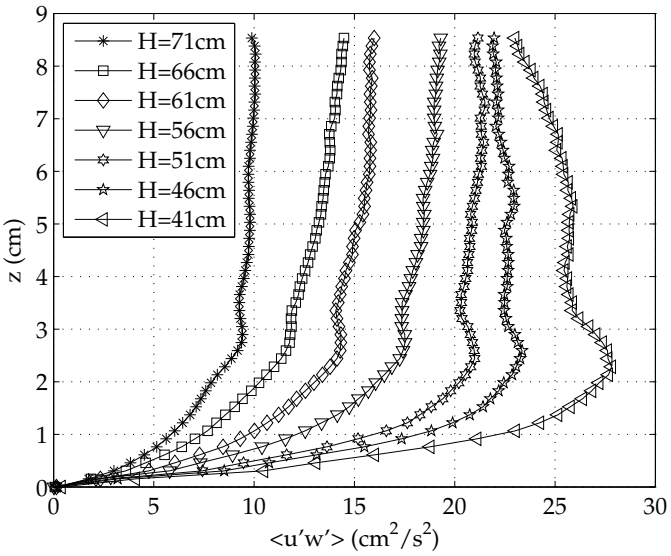

Figure 5.9: Weighted averages of Reynolds stresses from quadrant analysis

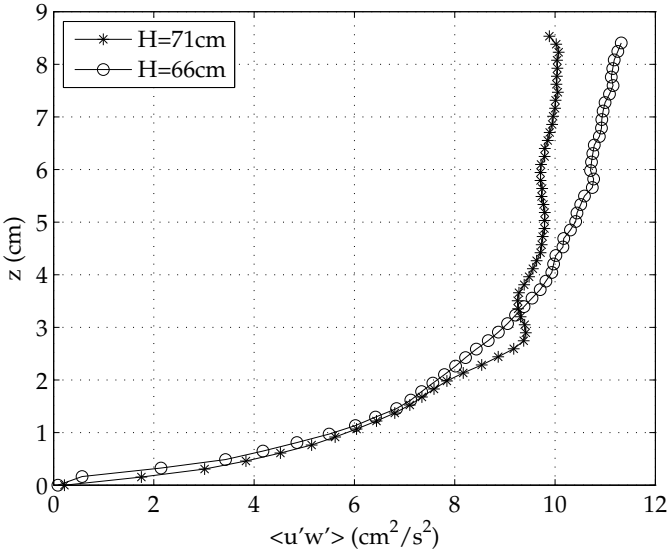

Figure 5.10: Comparison of weighted averages for sand and glass beds

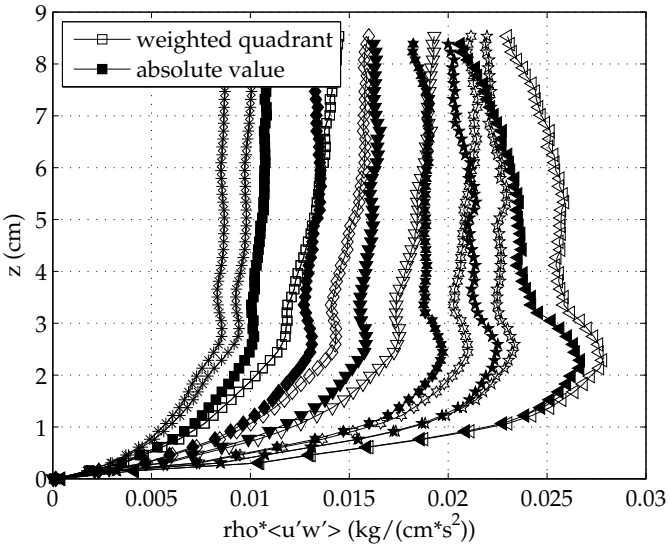

Figure 5.11: Comparison of Reynolds stress absolute value and weighted averages

and $\overline{w'w'}$ profiles shown in Figure 5.4, increasing in magnitude as RASJA height increases, with evidence of a boundary-influenced layer within 3cm of the bed in the solid boundary cases, and a very smooth growth profile of $\overline{u'w'}$ with the sediment boundary. Though we might expect a maximum $\overline{u'w'}$ value in the bed-influenced region, followed by a decay in Reynolds stress in upper heights, as is typical in channel flow boundary layer theory, we do not see this structures with a sediment boundary. The bump is still evident in Figure 5.5, though the Reynolds stresses also grow above this boundary-influenced height.

The shapes and magnitudes of the curves are noticeably similar between the four quadrants, obviously varying with jet height and type of bottom boundary. In the cases of the solid glass boundary, it is easy to see more jagged profiles, whereas the smoother sediment profiles omit the bump feature, or enhanvement of Reynolds stress, in this particular analysis. As is highlighted in Figure 5.12, a pattern emerges when comparing the profiles from each quadrant at any

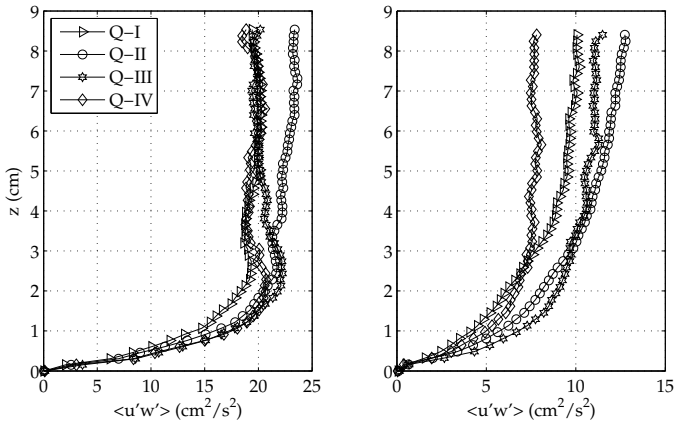

Figure 5.12: Reynolds Stress: Quadrant Comparison for Solid Boundary (H=51cm) and Sediment Boundary (H=71cm)

given boundary condition. Only two trials are shown in Figure 5.12, though they are consistent with the profile shapes for all of the other experiments, regardless of boundary condition or jet height.

Profiles from quadrants I and IV are of smaller magnitudes than profiles from quadrants II and III, suggesting greater velocity fluctuations in the leftward x-direction in this particular FOV. Also, profiles in quadrants I and II show more enhanced stresses from 2-3cm above the bed, with a steep $\overline{u'w'}$ magnitude gradient near the bed, compared to the smoother profiles of quadrants III and IV that show smaller magnitudes near the bed and gradually increase away from the bed. The differences in shapes occur when the vertical velocity fluctuation shifts from positively-valued to negatively-valued, which implies differences in behavior as flow approaches the bed or is ejected from the bed, hence an antisplat that is not a true opposite of a splat. These two flow patterns are apparently not reversible, as the direction of fluid particles determines which Reynolds stress profile will dominate. Notably different Reynolds stress gradients prevail when particles are either ejected from the bed or flow toward it.

Several generalizations about the flow can be made by comparing the quadrant Reynolds stress profiles. In a flow comprised of horizontally homogeneous turbulence with negligible secondary flows, we would expect that Reynolds stresses calculated from positive horizontal fluctuations should be equal to those from negative fluctuations, such that statistics in quadrant I are equal to statistics in quadrant II. While there is a slight discrepancy in magnitude, we do observe similar shapes. This also implies that quadrants III and IV should show similar behavior, and indeed again show small magnitude variations but very similarly shaped profiles. The offset in magnitudes is likely due to the FOV placement being slightly off-cener or possibly tilted, and therefore not fully symmetric, due to local inhomogeneity in the horizontal that is evident also in the spatial velocity field data, as presented in Figure 3.2. However, in the construction of single profiles, we maintain the assumption of horizontal homogeneity and continue to average across the horizontal PIV FOV.

5.3 Resuspension Structures and Stress Analysis

With the raw photos from the PIV data, we have the ability to consider resuspension and stresses by selecting images that show sediment entrainment, and investigating differences between images in which sediment remains on the bed. Thus, we can consider scatterplots in a more focused manner, and attempt to further understand physical mechanisms of resuspension.

In Figure 5.13, we compare velocity fluctuations selected from 48 PIV image pairs, half of which showed sediment resuspension (left), and half of which did not (right). Local regions of interest in the FOV were selected for the 24

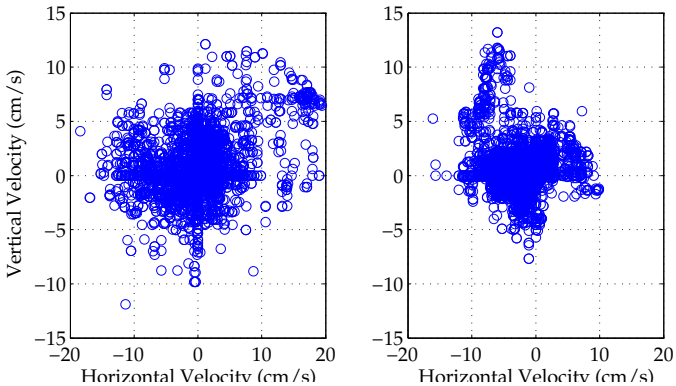

Figure 5.13: Scatterplots of resuspending and stationary bed events

image pairs that focused upon the local region of the image that specifically showed entrained suspended sediment, depending on the individual image. Comparable regions of interest were selected in corresponding image pairs in which resuspension was not observed, so that the scatterplot with resuspension could be compared to a baseline scatterplot that represents turbulent flow above a stationary sediment boundary, in a much more bed-focused region than was presented in Figure 5.6. Comparing the two plots, we notice a significantly greater range in fluctuations when sediment is entrained in the flow, with horizontal velocity fluctuations near 20cm/s and vertical velocity fluctuations up to 12 cm/s, compared to 12cm/s and 10cm/s horizontal and vertical fluctuations, respectively, in the scatterplot without suspended sediment. We notice differently shaped scatterplots, such that there is greater spread in quadrant I for suspension, whereas quadrant II shows a high concentration of velocity fluctuations absent suspension.

It must be noted that the scatterplots in Figure 5.13 likely do not show velocity fluctuations associated with incipient sediment motion, but simply capture sediment resuspension episodes that traveled through the FOV at some point in a 5-20 second event duration. Unfortunately we cannot truly compare incipient

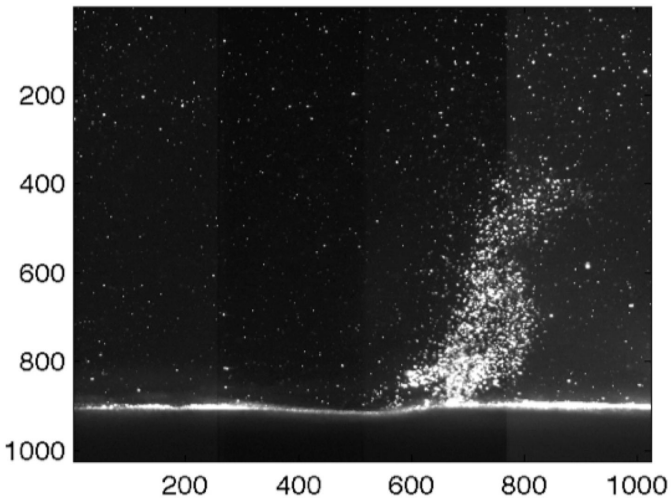

Figure 5.14: PIV Image of Sand Vortex

motion to either entrained sediment data or data absent suspension since we do not know when the data precisely show incipient motion, but this analysis helps to identify necessary flow parameters for sediment motion.

Within the first thirty minutes of testing, the majority of the bed remained fairly flat and even (as shown previously in Figure 6.1). Vertical resuspension events were observed, in which sand grains were picked up in vortices 1-5cm in height. Once the sediment was picked up into a vortical structure, the vortex traveled laterally across the surrounding flat regions of sand in the tank for several seconds until settling back out. An example of a vortex traveling through the PIV FOV is shown in Figure 5.14, in which the axes shown the pixel locations in the 10cm FOV.

The other dominant resuspension mechanism was the splat, observed as bed-parallel sediment motion traveling radially outward from a given center location. These events were highly three-dimensional, and therefore difficult to capture in a single FOV, though Figure 5.15 shows an example of this phe-

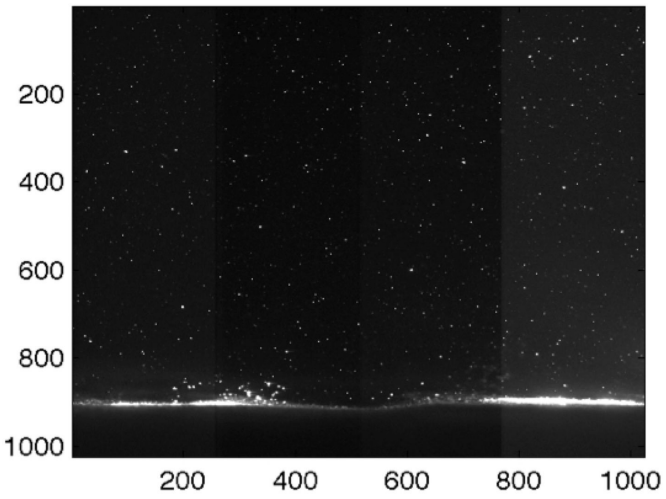

Figure 5.15: PIV Image of Sand Splat

nomenon with sand grains raised only slightly above the bed.

One method that was attempted to determine a critical stress for sediment resuspension was to track the progression of stress values with values of light intensity of the raw PIV images. During sediment resuspension events, the grains of sand that pass through the FOV are illuminated very brightly, and cause a significant increase in image intensity during the Matlab image pair analysis. Thus, a time history of image intensity would highlight resuspension events; if a threshold minimum intensity were determined as evidence of definite resuspension, then the associated time history of stress would likewise show the critical stress for sediment motion. We would expect stress peaks to slightly precede intensity peaks, as an elevated stress event would cause resuspension, and it might take several seconds for the suspended cloud of sediment to pass through the FOV.

In Figure 5.16, an example of these time histories is presented. The image intensity was not computed for the entire 10cm FOV, but instead in a limited

region approximately 3cm above the bed, within which the greatest sediment resuspension occurred. Several heights closer to the bed were examined and yielded similar results. The intensity has been scaled to magnitude of the bed stress. The absolute stress is the combined viscous and Reynolds stress terms, taken as the maximum total stress value at a height of 3cm above the bed, where we expect significant stress events due to the location of the maximum stress bump in the conditional averaged Reynolds stress analysis, with close to zero contribution from the viscous term. The weighted stress history term is taken as the absolute value of the Reynolds stress term, also taken at a height of 3cm above the bed. Unfortunately, with this analysis (and several other attempts with alternate locations of stress and different areas over which intensity was summed, including regions immediately above the bed in which we may see viscous stresses), we do not see the trend that was expected. The stress peaks do not precede the intensity peaks, and show no significant correlation otherwise. This method seems promising, but with the current analysis scheme, does not provide insight into the critical stress and resuspension events.

5.4 Non-Dimensionalized Boundary Layer Profiles

5.4.1 Scaling Analysis

After computing metrics of the flow such as turbulence intensity, dissipation, and Reynolds stresses, it is valuable to find parameters by which the aforementioned profiles can be made non-dimensional and, ultimately, universal to all homogeneous isotropic turbulent flows. In this analysis, we choose to scale ve-

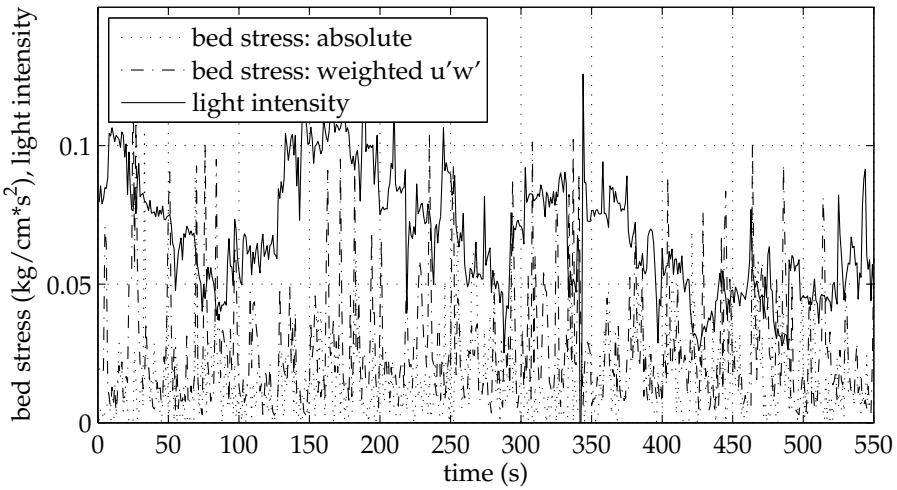

Figure 5.16: Time history of PIV image intensity and bed stress, calculated according to both the absolute and weighted Reynolds stress methods

locities by $u_{*,cr}$, the friction velocity. Previously, the friction velocity was defined according to the bed stress. As we found that bed stress cannot be computed through traditional methods in this facility, an alternate friction velocity is being used such that

$$u_{*,cr} = \sqrt{|\overline{u'w'}_{max}|}$$

This maximum Reynolds stress will be taken from the weighted averaged Reynolds stress plot in Figure 5.9 in the bed-influenced region.

Length scales will be scaled by L_u, the integral length scale as computed from the autocorrelation function. Table 5.1 summarizes the value of the scaling parameters used at each boundary condition and RASJA height. The uppermost value has been selected as the representative integral length scale.

	L_u (cm)	L_w (cm)	$u_{*,cr}$ (cm/s)
Glass, H=71cm	7.447	7.172	9.42
Glass, H=66cm	7.780	8.424	11.87
Glass, H=61cm	7.381	6.749	14.32
Glass, H=56cm	7.169	6.793	17.52
Glass, H=51cm	6.681	6.234	21.00
Glass, H=46cm	4.408	6.152	23.36
Glass, H=41cm	4.475	6.775	27.82
Sand, H=71cm	7.821	7.108	8.87

Table 5.1: Scaling Parameters

5.4.2 Non-dimensional Profiles

After scaling the Reynolds stresses $\overline{u'u'}$, $\overline{u'w'}$, and $\overline{w'w'}$ by the values of L_u and $u_{*,cr}$ presented in Table 5.1, Figure 5.17 shows the resulting non-dimensional plot. The data from all eight files is presented here, from the seven different jet heights above a glass bed, and maximum jet height above a sediment bed. The curves collapse fairly well, though there are still some discrepancies, particularly in the $\overline{w'w'}$ profile in the profiles for the lowermost RASJA heights where the homogeneity of the turbulence is doubtful. Scaling other profiles such as turbulent kinetic energy, mean velocities, and turbulence intensities are a bit redundant and show equivalent degrees of collapse with these scaling parameters, so they have not been included since the Reynolds stress scaling seems sufficient.

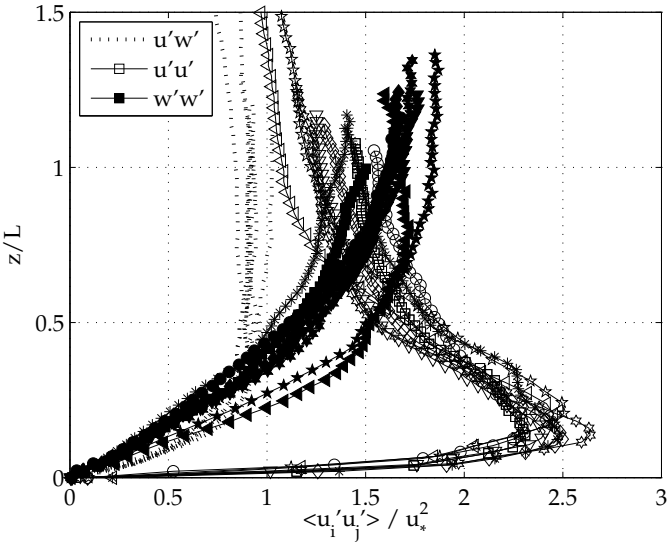

Figure 5.17: Reynolds stresses scaled by friction velocity and integral length scale

CHAPTER 6

SEDIMENT RESUSPENSION AND BED MORPHOLOGY

Running the default jet configuration, with 12% of jets running with a mean on-time of 3 seconds and the RASJA mounted at the maximum height above the bed, the level of turbulence generated was sufficient to resuspend sediment at the bed on occasion. In addition to entraining sediment into the flow during local resuspension events, the fluid structures also moved sediment along the bed, generating ripples and patterned structures of sand. Prior to each test with turbulence forcing, the sand was combed to be as flat and as smooth as possible so that departures from the smooth initial state could be monitored. Although a rigorous analysis has yet to be performed on the bed morphology and its response to varying turbulence conditions, the observations presented in this chapter serve to describe the novel finding and to provoke additional studies that will increase our understanding of the formation of ripples in decaying isotropic homogeneous turbulence above a sediment bed.

6.1 Mechanisms of Resuspension and Bed Deformation

During operation of the turbulence tank, two prominent mechanisms for sediment resuspension were observed: the vortex and the splat, images of which were shown in Section 5.3. These two phenomena are very different in shape and duration, and they have dramatically different impact areas as they leave behind footprints of their occurrences. They can occur together or individually, and observations of their frequency and role on bed deformation (and conversely, the role of bed deformation on their frequency) help us to understand the fluid mechanisms responsible for these events.

Starting from an initially flat bed, very small dimples in the sand began to appear within 15 minutes of turning the jets on, in regions away from the boundaries. To the naked eye, there were not sediment resuspension events that appeared to create these initial ripples, but we suspect that local splat-like or saltation-like events occurred as fluid directly impinged upon the bed. Across regions of the bed in which the sand remained fairly flat and smooth, often in the center of the tank, the first resuspension events observed were the vortices. These events did not occur with great frequency, perhaps one vortex every 2-5 minutes. Each vortex remained for up to 10 seconds. Small trails of their paths remained on the nearly-flat bed immediately after the vortex passed and small piles were formed as the sediment settled out of suspension, but these minor bed deformations did not contribute to the formation of ripples or large-scale sediment transport, as the trails and sediment piles were quickly smoothed away into the dominant large-scale emergent bedforms. At times, the vortices were not connected to the bed and left no path evidence prior to settling back into the bed. After a few hours, the bed was significantly deformed into a rippled pattern, with no remaining broad flat regions of sand. During this time, the presence of vortical resuspension events dropped significantly, as there were no broad smooth expanses of sand over which the vortices could travel.

As the turbulence continued to develop, the initial small-scale local ripples grew in size and spread until the entire bed was deformed into an organized grid. A summary of the bed deformation is presented in Figure 6.1 across the 12-hour record. The images are lit externally from the right side, so that peaks are often highlighted and troughs are emphasized in the shadows.

As the ripples grew to cover the entire bed, vortices were not observed in

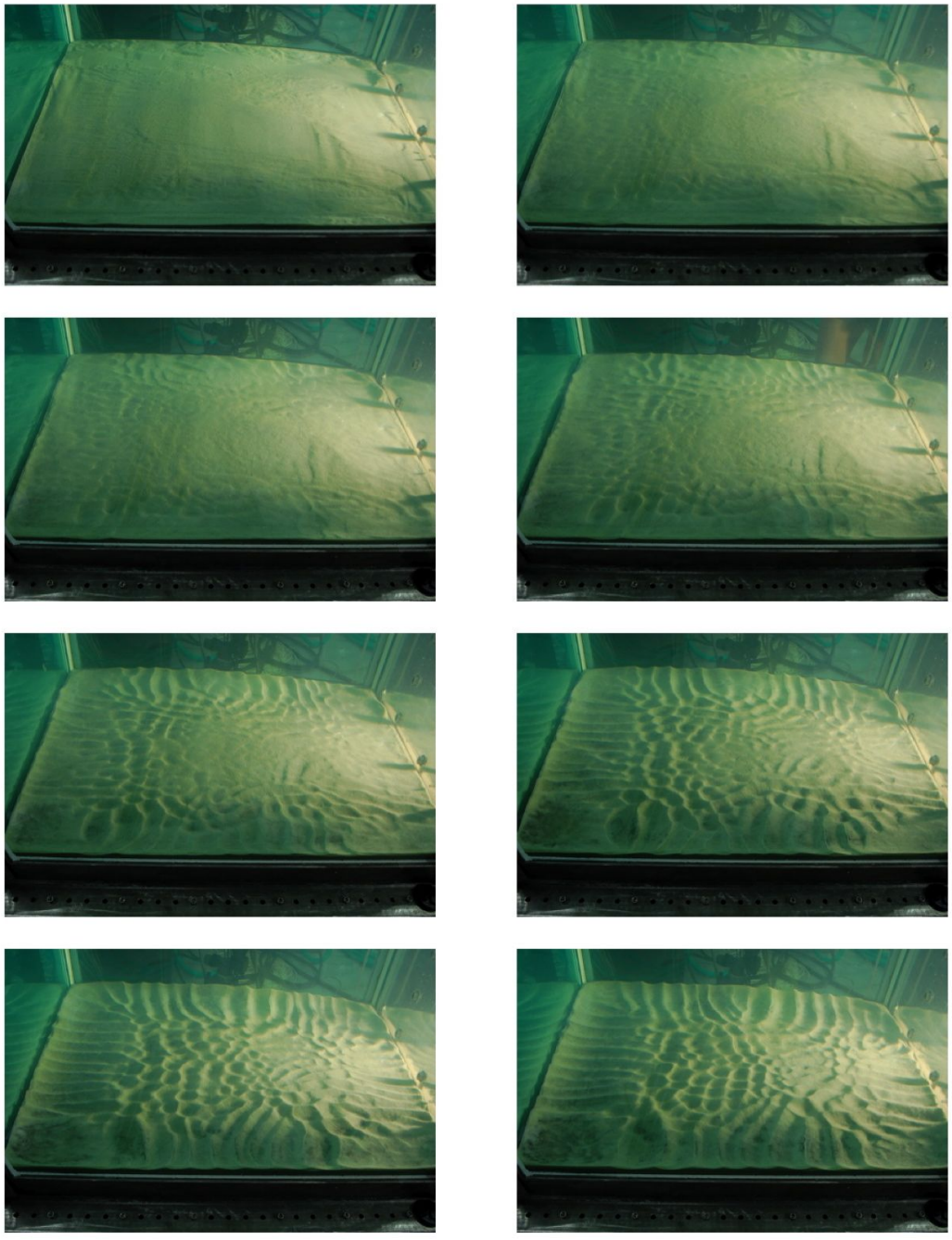

Figure 6.1: Evolution of Sand Bed at: Initial state, 15 minutes, 30 minutes, 1 hour, 2 hours, 4 hours, 8 hours, 12 hours

the default jet-firing state. Instead, resuspension was dominated by splats. During a fluid splat of significant strength, large quantities of sand were observed traveling parallel to the bed, moving radially outward from the center of the splat. These events tended both to deform the bed into ripples, and also to occur over rippled (as opposed to initially-flat) regions of sand. Sand grains were often moved up to 10cm from their starting locations during these events. Splats were responsible for scouring deeper ripple troughs and for influencing the migration of ripple peaks.

The splat resuspension events were typically more three-dimensional than vortical resuspension events, carrying sediment great distances in the x- and y-directions as it was elevated mere millimeters above the bed in the z-direction. Sediment was only briefly entrained in the flow before being deposited in its new location. Though sediment was only slightly lifted above the bed in the vertical, the entire process resulted in prominent bed deformations in the vertical. Furthermore, the splat resuspension events occurred more frequently on the rippled outer regions of the bed, and not as frequently in the center of the tank where PIV images were recorded until the bed had been significantly deformed, long after the 30 minute PIV record had concluded.

6.2 Ripple Spacing and Time Scales

Beginning from a smooth bed, the initial deformations in the sand appear to be small dimples, approximately 1-2cm across, and only a few millimeters deep. They are very local structures, seemingly randomly placed, and can be detected within the first 15 minutes of turning on the jets. These small dimples migrate

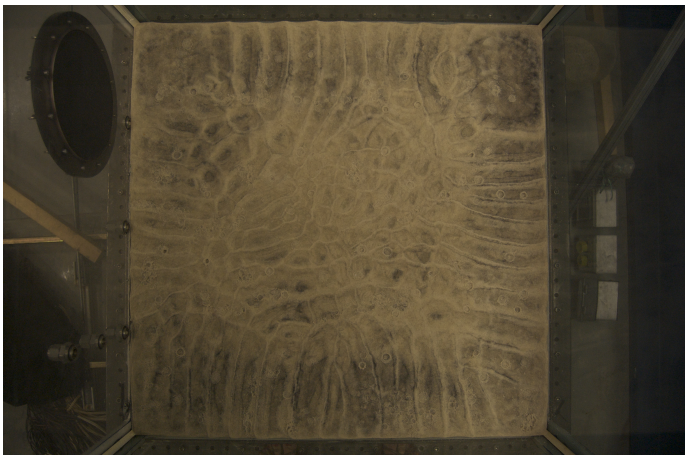

Figure 6.2: Equilibrium Ripple Spacing at 12 hours

about the tank and form a rather organized pattern approximately one hour into the experiment, though the ripples continue to grow into larger, more regularly shaped ripples until approximately two hours into the experiment, when they appear to reach their equilibrium size. The gaps in the pattern are filled in with equivalently sized ripples for the next two hours, until the entire sand bed has evolved into a rippled pattern. At this stage, the equilibrium ripple spacing, the length scale with which we are concerned, is approximately 5.1cm, found by computing the spectra of the image intensities across the row to obtain the ripple peaks, denoted by lighter-colored intensities. This equilibrium spacing is shown in Figure 6.2, a photo of the bed taken after a 12-hour period.

The wall-normal boundary ripples are very regularly spaced, reaching nearly 16cm into the center of the tank, with 1 cm differences in height between the crests to the troughs. The corners alternate between being vacant squares or continuations of the striped pattern, seemingly dependent upon the initial state of the sand. The distances between the crests are on the same order as the interior ripple spacing, as individual wall-normal ripples can be traced the entire length across the bed.

6.3 Side-Wall Boundary Effects

In the default jet firing configuration, with 12% of all jets operating on average, the observed ripple pattern is ostensibly different near the edges of the tank than it is in the center. Ripples are aligned normal to the boundaries and migrate toward the center of the tank. As two parallel ripples migrate towards each other in the center of the tank, they ultimately merge into a new central ripple. The outermost ripples are replaced by new ripples, and a consistent size and spacing pattern is maintained. While ripples and bed deformations were initially created in the center of the tank, away from the boundaries, they are of a different structure than the equilibrium striped edge ripples, as there are overlapping regions of ripples that instead form an orthogonal grid.

Variano's research in this facility computed an integral length scale of 7.57cm, and it was noted that the turbulence was not fully homogeneous within two integral length scales of the wall (Variano and Cowen, 2008). This is consistent with the observation that the bed pattern varies visibly within 16cm of the wall. We find a consistent integral length scale of 7.8cm above a sediment bed. Suspecting that there might be secondary flows near the boundaries, we performed an ADV measurement 10cm above the bed and 8.6cm away from a wall but saw less than 5% mean flow strength, as was presented in Figure 3.6. Though this ADV mean flow measurement suggests there are not significant mean flow patterns near the wall. A more thorough near-wall examination has not yet been performed.

Though we do not yet fully understand the difference between wall ripples and interior ripples, we attribute their formation to the turbulence. We expect

that the ripples do not exist because of the presence of boundaries, but simply that the orthogonality is a consequence of the square tank and the no flux boundary condition. Thus we hypothesize that in an infinite boundless tank, the rippled pattern would still exist and extend across the infinitely large sediment interface, but we would not see the orthogonality imposed by the side walls. This is investigated further in the following sections.

6.4 Interior Solid Obstacles

After watching the ripple development and time-lapsed photographs of the growth patterns, it was hypothesized that perhaps the ripples were only formed because there were side boundaries in the tank that forced the fluid to interact in such a way to create organized orthogonal patterns, even though the first ripples that appeared were not connected to the walls.

Suspecting that this was not true, that indeed in an unbounded tank with infinitely many jets we would see the same interior orthongal ripple bed, a test with a small interior solid "boundary" was performed, in which a solid metal cube was placed in the tank, sitting on the surface of the sand. If the ripples existed only because of fluid interactions with walls, then we expected to see ripples growing off of the cube faces, just as wall-normal ripples had grown along the sides of the tank.

Instead, there appeared to be no change in the growth of ripples due to the presence of the solid cube in the tank. Ripples grew perpendicular to the side walls, while the interior was filled with a grid of ripples, similar to the default test. The difference that was observed was that as ripples surrounded the cube,

they also scoured out sand beneath the cube, causing it to tip over several hours into the test. The scour holes appeared to be deeper than the troughs of surrounding ripples. Thus we did note altered fluid behavior and a different degree of resuspenion near the cube, since sediment could be resuspended and carried away perhaps more easily than it drifted back in to fill the holes, though we did not perform further studies on fluid/sediment interactions with other interior structures. We note that this has interesting implications for foundation systems in the presence of high levels of turbulence.

6.5 Observed Resuspension with Alternate Firing Patterns

6.5.1 Elimination of Outer Jets

In an attempt to determine whether ripples could form in absence of side boundaries, or whether the resulting orthogonal grid would exist in an "infinite" system, tests were performed in which the turbulence was, in essence, isolated from the side walls, by turning off the jets that fire in the outer perimeter(s) of the RASJA. In one test, a 6x6 interior grid of jets was fired with the same 12% algorithm as used previously, and in the other test, a 4x4 interior grid was run. PIV data were not collected during these tests, as this was just a simple observational study at this point in the research, but vertical velocity profiles were recorded with the Aquadopp HR Profiler as discussed previously in Chapter 4.

In each case, a patterned ripple grid was observed in the center of the tank, similar to the interior ripple grid observed in the default jet firing configuration. The size and spacing of the ripples were similar to those of the equilibrium

ripples, however an equilibrium state could not be achieved in these test cases, since the lack of jet-firings from the outer perimeters caused sand to be dug out of the center and pushed towards the side walls, without the balance of all jets running. No wall-normal ripples along the boundaries were formed; the only structures noted near the walls were some wall-parallel dunes that were the result of large-scale sediment transport from the turbulent interior of the tank to the unforced outer jet perimeter above the bed. A photo of the resultant ripples is shown in Figures 6.3 and 6.4, taken after two hours of running the 6x6 and 4x4 jet arrays, respectively. Though the ripples fell into a regular pattern, there was no strict orthogonality, nor replacement of migrating ripples as was observed in the default 8x8 firing.

Furthermore, we noticed that the elimination of the outermost jets affects the direction of the mean flow through the center of the tank. We expect more significant return flows near the walls in these experiments, as noted previously. However, despite these changes in the bulk flow patterns, we observed very similar ripple evolution patterns emerging at the bed, thus it is indeed most likely the turbulence that is responsible for bed morphology, and not necessarily the physical structure of the tank at large.

From these observations, it seems that the walls are not essential to the creation of ripples, and that surely the ripples do not physically originate at the walls before spreading into the center to create patterned intersections. While the boundaries may indeed play a role in determining the scales of the turbulence present and the orientation of the ripples, it is indeed the turbulence creating the ripples, and not precisely the placement of walls in a turbulent field.

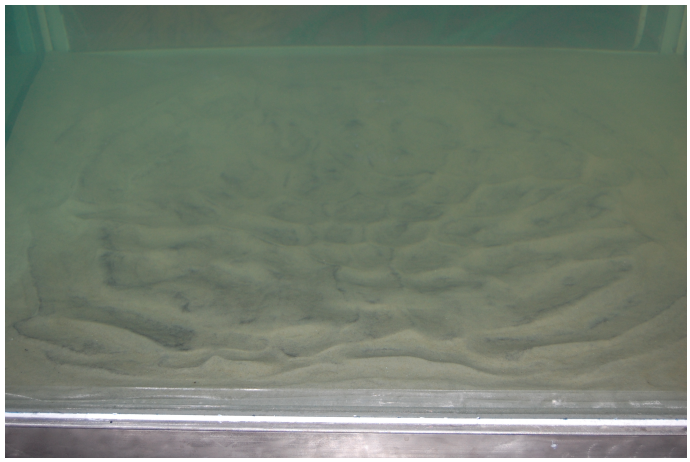

Figure 6.3: Resulting ripple pattern from 6x6 array of jet firing

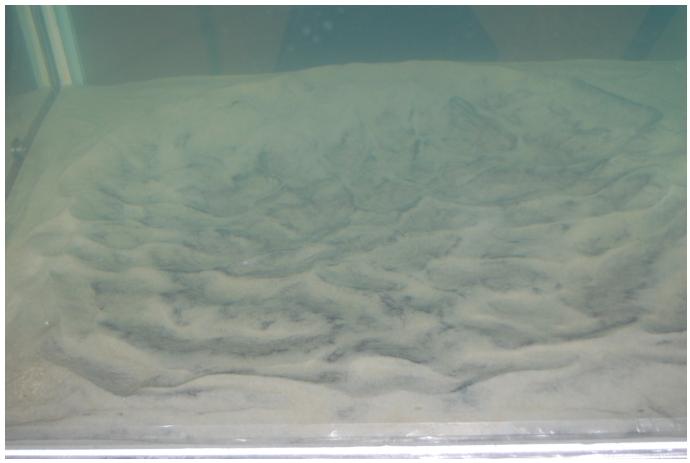

Figure 6.4: Resulting ripple pattern from 4x4 array of jet firing

6.5.2 Increased Jet Spacing

A trial was performed in which 25% of the jets were selected to run on the random firing algorithm, such that the RASJA was treated as a large 4x4 grid instead of an 8x8 grid. No adjacent jets fired, and the rows of jets remained orthogonal to the tank walls. The 12% firing algorithm of the selected 16 jets was maintained as in previous tests.

In this configuration, the bed deformed into a very simple 4x4 ripple grid,

such that the trough of each ripple was reasonably centered between the operating jet above. From this observation, we concluded that there was not enough height in the tank relative to the jet spacing for the jets to merge into the layer of homogeneous isotropic turbulence that was observed when adjacent jets were operational. With a 20cm jet spacing, we would need a depth of 120cm between the RASJA and the bed. The jet merging region had not yet formed, and the flow at the base of the tank was heavily influenced by the on/off state of the closest jet. There was indeed sediment resuspension, and turbulence in the flow, but this was an inconclusive test in examining sediment boundary morphology from well-mixed turbulence.

6.6 Observed Resuspension with Varied RASJA Height

In order to determine how the resuspension events might change in response to different levels of forced turbulence, experiments were performed in which the RASJA was lowered closer to the bed in 5cm increments, from 71cm to 41cm between the jets and the sediment bed, using the default jet firing algorithm in every case. The observed bed deformations were quite surprising, both in the resulting ripple patterns and the methods of resuspension observed.

6.6.1 71cm Jet Height

The uppermost jet height is the default condition described previously. In this case, vortices are observed forming and traveling across regions where the sand is flat. Ripples start forming near the side boundaries, and are formed and af-

fected by the interaction of splats and anti-splats. Thus as the turbulent forcing continues and ripples reach into the center of the tank, the flat regions are overtaken by ripples, vortices no longer form, and bed deformation and ripple migration occurs through splat events, both in the interior ripple grid and along the wall-normal boundary ripples.

6.6.2 56-66cm Jet Heights

As the jet array approaches the bed by 5-15cm, similar patterns are observed, in which there are wall-normal boundary ripples, small vortices for a short period of time at the beginning of the experiment, and large splats dominating deformation of the ripple grid in later time. The orthogonal ripple grid is generally formed in the same manner regardless of jet height. The time over which the bed evolves is affected, as resuspension more readily occurs and bed features evolve more quickly with low jet heights when the forcing is nearer the bed as compared to the imposed initial condition.

6.6.3 46-51cm Jet Heights

At a jet height of 51 cm, the third-lowest height tested, notable differences were observed in the sediment bed structure. Larger scale orthogonal ripples began forming, in which there was an overall 4x4 grid of ripple troughs, separated by 3 ripple crests in each direction that traversed the entire length and width of the bed. Within this overall 4x4 ripple grid, some of the squares along the boundary showed the same wall-normal ripples that had been observed previously,

whereas other squares showed no coherent structure within, corner squares included. In the interior four squares, small orthogonal ripple grids similar to the previous interior structures were visible. At times, they merged into striped ripple crests, and at other times, they were filled with irregular structures.

There was a much greater frequency of splats throughout the tank, with at least one splat every 2 seconds. Sometimes, five or more splat-induced resuspension events were visible simultaneously. Suspended clouds of sediment that resulted from splats thus had opportunities to interact, and it was observed that clouds of sand passed through one another, instead of evolving into anti-splat or more dramatic bed-ejection events. With this greatly deformed bed, vortices were not expected, based on the original observation that vortices occur only over flat bed conditions. However, many short-lived vortices were observed at the intersection of splats, lasting less than 2 seconds each. Sometimes they grew to heights up to 5 cm above the bed, and at times they were completely detached from the bed, leaving no trail of their path behind, except for a small pile of sand that fell out of suspension when the vortex stopped rotating. Often, it appeared that vortices could increase their sediment content and duration after interacting with a nearby splat that perhaps injected additional sediment into the rotation or energy that allowed faster rotation and the ability to resuspend new sediment from the bed. Vortices occurred both over ripples and over smooth areas in this trial, unlike previous observations at maximum jet elevation.

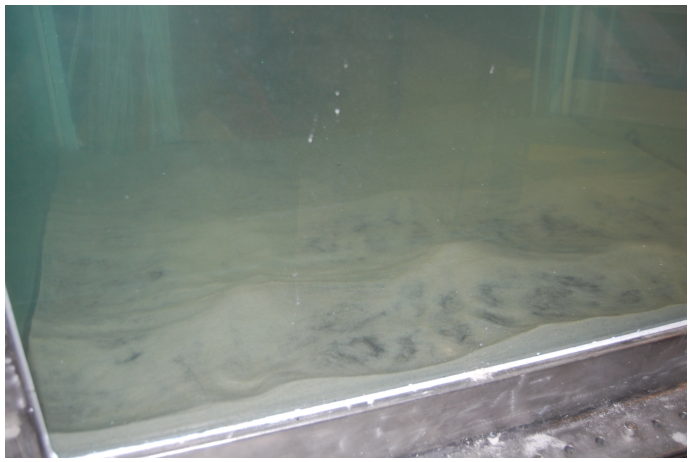

Figure 6.5: Resulting ripple grid with lowermost (41 cm) jet height

6.6.4 41cm Jet Height

At the lowest RASJA height tested, 41 cm, the sediment bed structure was completely dominated by the 4x4 grid of large ripples, with no visible history of the small wall-normal or interior intersecting grid ripples that had previously formed. Very large peaks occurred at the intersections of the 4x4 ripple grid, with heights near 6cm above the adjacent troughs. The crests migrated locally due to the high frequency of splats, but remained rather evenly spaced across the tank. The loss of small ripples promoted long durations of vortex events, which sometimes interacted with splat resuspension events, and at other times, seemed to form in absence of resuspension-inducing splat events. A photo of this pattern is shown in Figure 6.5.

The resulting 4x4 ripple grid was similar to that described in Section 6.5 with only 25% of the jets firing, where it was formerly evident that the jet flows had not merged into homogeneous turbulence. However, in this case, with the entire 8x8 jet grid operational, there perhaps is a jet-merging region in this configuration, despite the low RASJA height of 41 cm. If the jet flows had not mixed, we

Figure 6.6: Close-up photo of RASJA, highlighting gaps between 4x4 jet clusters

would have observed an 8x8 rippled grid in this instance, with troughs centered beneath each individual jet orifice, but instead, the sediment formed an unexpected larger-scaled 4x4 structure. Small ripples remaining in the initial condition from previous tests were immediately erased, and this 4x4 ripple structure clearly dominated early in the process, as a result of either the turbulence, the tank shape itself, or some conbination thereof that has yet to be determined.

A possible explanation for this dominant 4x4 grid comes from the details of the tank geometry. Though the jets are arranged in an 8x8 grid, they are structured in clusters of 4 jets per cluster, such that the jet motors and bilge pumps occupy space in the clusters. As shown in Figure 6.6, there are no "fillers" between each cluster, even though the jet orifices are evenly spaced, regardless of whether there is a jet motor in between two adjacent orifices.

Because of these gaps between the 4x4 array of jet clusters, there is space for return flows, as water needs to flow upward to feed the bilge pumps that supply the jets. We have not yet performed detailed tests near enough the RASJA to determine whether this is the culprit for the 4x4 ripple grid, though it seems

reasonable considering the proximity of the RASJA to the sediment bed. If this is a problem, that the structure of the tank is indeed influencing sediment resuspension and the behavior of the turbulent flow, a possible solution would be to suspend a sheet in the plane of the jet orifices, with holes at each orifice for the jets, and with additional perforations for evenly distributed return flows to the bilge pumps.

CHAPTER 7

CONCLUSIONS

7.1 Analysis

After configuring the turbulence tank into a facility designed to study the decay of homogeneous isotropic turbulence at various bottom boundaries, we can summarize findings regarding tank performance, turbulence decay at impermeable and sediment boundaries, and the impact of turbulence on sediment bed morphology. By using several different instruments and measurement techniques simultaneously in each experiment, we can compare the performance of each instrument in a highly turbulent flow, as each instrument captures different metrics that are essential in characterizing the flow and boundary layers.

In the initial tank characterization experiments, the RASJA was suspended 71cm above the bottom glass boundary, and the jet-firing algorithm from Evan Variano (Variano and Cowen, 2008) for maximum turbulence generation and minimum mean current was used. ADV measurements were recorded throughout the entire height of the tank, and PIV measurements were recorded within 10cm of the bed. With both measurement sets, we see very low mean velocities, and more notably, mean flow strengths of less than 10% in the bottom 30% of the tank. Mean velocities are as high as 2cm/s in the vertical and horizontal in the particular measurement regions selected, but appear much less significant than the velocity fluctuations that arise in localized turbulent structures.

We note differently shaped profiles of mean horizontal and vertical velocities, turbulence intensity, and other metrics, and treat the flow as horizon-

tally homogeneous turbulence that decays in the vertical as it approaches the bed. Particularly in the measurements above the solid glass boundary, a bed-influenced region is evident, as pronounced enhancements are apparent in the turbulence intensity and kinetic energy profiles, approximately 3cm above the bed. Though this feature is not observed in the case of turbulence above a sediment boundary, as energetic bed-normal fluid can penetrate the boundary instead of being converted from the bed-normal to bed-parallel direction, we see physical evidence of the kinematic boundary effect in sediment resuspension events and bed deformation.

Temporal spectra computed from ADV measurements show a long inertial subrange, with a slope of -5/3 when plotted on a log-log scale, and spatial spectra computed from PIV measurements also show satisfactory agreement with turbulence theory. From the velocity spectra and autocorrelation function, we can compute dissipation and integral length scales of the turbulence. Though we see differences in magnitude of the dissipation plots, depending on the methods used to compute the profiles, we see similar profile structures between glass and sediment beds. There are distinct differences whether the profiles were computed from bed-parallel or bed-normal velocity records, as we do not have fully isotropic turbulence at the bed, yet we assume isotropy in the calculations. The best agreement between the profiles computed from the different components of velocities is closest at the uppermost locations in the FOV, distant from the bed, where the flow is nearly isotropic. With more refined measurements over larger spatial fields, the dissipation profiles might be improved. Additionally, recording data at a higher frequency near the bed would enable dissipation to be computed from temporal spectra, which has not yet been attempted. The autocorrelation function is used to calculate the integral

length scale, which is an important parameter in this facility, as we use this as a scaling parameter. Typical viscous lengthscales are not particularly relevant in this facility, and so we ultimately aim to alter the states of turbulence via the integral length scale to determine the applicability of our findings to other highly turbulent flows.

As we are unable to find meaningful bed stress parameters with traditional boundary layer theory, we look to Reynolds stresses to investigate the local structures responsible for sediment resuspension and general near-bed flow dynamics. By performing quadrant analyses on the PIV data, notably different profiles are observed whether fluid parcels approach the bed or are ejected from it. Scaling the Reynolds stresses with a new friction velocity defined from the quadrant-averaged Reynolds stress and the integral length scale results in profiles that collapse fairly well, though additional tests will be required to determine whether these are the proper scaling parameters regardless of the turbulent forcing above the bed.

Tests were performed with the RASJA positioned at varying heights in order to observe differences in boundary layer profiles due to altered states of turbulence. Above the solid glass bed, enhanced turbulence intensity in the bed-parallel direction was significant as the jets approached the bed, as there was less distance over which the turbulence could decay towards the bed. With a sediment boundary in place of the glass boundary, tests were completed with different RASJA heights, but measurements were only recorded during the test with the uppermost jet height. Observations showed that a shorter distance between the jets and the sand (and thus a smaller volume over which the turbulence could evolve) created a much more dynamic bed, with greater quantities

of sediment resuspension and entrainment in the flow directly above the bed than were observed with more distant jet heights.

The two observed mechanisms of sediment resuspension include vortices and splats. Though these mechanisms contributed to sediment transport and, at times, enhanced features along the rippled sediment bed, it seems that resuspension was not essential to bed morphology. Although the organization of the ripples may be influenced by the particular shape of the tank and jet spacing, we believe the ripples exist because of the presence of turbulence. The initial formation of ripples does not begin along the tank walls, and it is only after a bit of time that the orthogonal pattern dominates the bed topography. The spacing of the ripples is equal to about half the value of the integral length scale of the turbulence. Although the preliminary ripple findings seem promising that they are a result of the interaction with decaying turbulence along the bed, many future tests involving altered boundaries and turbulence generation will be required to investigate this phenomenon more thoroughly.

7.2 Future Work

As this project continues to develop, the most important feature involves altering the generation of turbulence more dramatically, in an attempt to alter the integral length scale and determine whether the current scaling parameters and boundary layer characterizations are universal and not simply functions of this particular laboratory setup. This can be completed by altering the physical geometry of the tank, and by programming the jets to operate with different firing parameters such that the on-off states of each jet change either more rapidly or

more slowly, or changing the average number of jets that fire at a given time. Better understanding the role of physical boundaries in the turbulent flow will be important not only in understanding the influence of tank structure on our results, but also in enhancing our knowledge of scour and other pertinent applications in civil engineering.

In addition to better understanding the boundary layer profiles, altering the turbulence levels in the tank will assist in understanding the role in sediment resuspenion and bed morphology. It will be crucial to identify the lowest Reynolds stresses for which we observe sediment resuspension. We must also determine the influences on ripple development, and identify how the kinetic energy and turbulence intensities affect the length and time scales of bed morphology. Increasing the levels of turbulence present in the tank will increase the frequency and content of sediment resuspension, and will further our understanding of sediment resuspension and entrainment in turbulent flows.

Ultimately, the goal of the research is to provide a parameterized shear stress that is essential to incipient sediment motion from the bed. More refined PIV measurements taken in more regions of the tank will help to further characterize the flow across the tank. By incorporating both PIV and PTV, we can better track sediment motion through the turbulent fluid separate from fluid motion. By tracking sediment grains and identifying local stresses in the flow responsible for resuspension, we can better understand the requisite parameters of turbulent flows that are essential for sediment transport, and we will thus be able to better predict which environmental flows may result in sediment resuspension and bed morphology, and predict the consequent scour and erosion that can result due to fluid interactions with sediment beds.

BIBLIOGRAPHY

Brumley, B. and Jirka, G. (1987). Near-surface turbulence in a grid-stirred tank. *Journal of Fluid Mechanics*, 183:235–263.

Cowen, E.A. and Monismith, S.G. (1997). A hybrid digital particle tracking velocimetry technique. *Experiments in Fluids*, 22:199–211. 10.1007/s003480050038.

Efron, B. and Tibshirani, R. (1993). *An Introduction to the Bootstrap*. Chapman & Hall.

Hunt, J. (1984b). Turbulence structure in thermal-convection and shear-free boundary layers. *Journal of Fluid Mechanics*, 138(JAN):161–184.

Hunt, J. and Graham, J. (1978). Free-stream turbulence near plane boundaries. *Journal of Fluid Mechanics*, 84(JAN):209–235.

Kolmogorov, A.N. (1941). The local structure of turbulence in incompressible viscous fluid for very large reynolds numbers. *Dokl. Akad. Nauk SSSR*, 30:299–303.

Liao, Q. and Cowen, E. (2005). An efficient anti-aliasing spectral continuous window shifting technique for piv. *Experiments in Fluids*, 38:197–208.

McKenna, S. and McGillis, W. (2004). Observations of flow repeatability and secondary circulation in an oscillating grid-stirred tank. *Physics of Fluids*, 16(9):3499–3502.

Medina, P., Sanchez, M. and Redondo, J. (2001). Grid stirred turbulence: Applications to the initiation of sediment motion and lift-off studies. *Physics And*

Chemistry Of The Earth Part B-Hydrology Oceans AND Atmosphere, 26(4):299–304.

Orlins, J. and Gulliver, J. (2003). Turbulence quantification and sediment resuspension in an oscillating grid chamber. *Experiments in Fluids*, 34(6):662–677.

Perot, B. and Moin, P. (1995a). Shear-free turbulent boundary-layers .1. physical insights into near-wall turbulence. *Journal of Fluid Mechanics*, 295:199–227.

Perot, B. and Moin, P. (1995b). Shear-free turbulent boundary-layers .2. new concepts for reynolds stress transport-equation modeling of inhomogeneous flows. *Journal of Fluid Mechanics*, 295:229–245.

Pope, S. (2000). *Turbulent Flows*. Cambridge University Press.

Redondo, J., de Madron, X., Medina, P., Sanchez, M. and Schaaff, E. (2001). Comparison of sediment resuspension measurements in sheared and zero-mean turbulent flows. *Continental Shelf Research*, 21(18-19):2095–2103.

Sanchez, M. and Redondo, J. (1998). Observations from grid stirred turbulence - grid characterization and application to sediment lift-off experiments. *Applied Scientific Research*, 59(2-3):243–254.

Teixeira, M. and Belcher, S. (2000). Dissipation of shear-free turbulence near boundaries. *Journal of Fluid Mechanics*, 422:167–191.

Thomas, N. and Hancock, P. (1977). Grid turbulence near a moving wall. *Journal of Fluid Mechanics*, 82(SEP27):481–496.

Thompson, S. and Turner, J. (1975). Mixing across an interface due to turbulence generated by an oscillating grid. *Journal of Fluid Mechanics*, 67(JAN28):349–&.

Tropea, C., Yarin, A. and Foss, J., editors (2007). *Springer Handbook of Experimental Fluid Mechanics*. Springer.

Tsai, C. and Lick, W. (1986). A portable device for measuring sediment resuspension. *Journal of Great Lakes Research*, 12(4):314–321.

Turner, J. (1968). Influence of molecular diiffusivity on turbulent entrainment across a density interface. *Journal of Fluid Mechanics*, 33(Part 4):639–&.

Uzkan, T. and Reynolds, W. (1967). A shear-free turbulent boundary layer. *Journal of Fluid Mechanics*, 28(Part 4):803–&.

van Rijn, L. (1984). Sediment transport, part i: Bed load transport. *Journal of Hydraulic Engineering*, 110:1431–1456.

Variano, E., Bodenschatz, E. and Cowen, E. (2004). A random synthetic jet array driven turbulence tank. *Experiments in Fluids*, 37:613–615.

Variano, E. and Cowen, E. (2008). A random-jet-stirred turbulence tank. *Journal of Fluid Mechanics*, 604:1–32.

Wereley, S. and Nguyen, N. (2002). *Fundamentals and Applications of Microfluidics*. Artech House Publishers.